

AD \_\_\_\_\_

CONTRACT NO: DAMD17-94-C-4052

TITLE: Development of a Novel Intravenous Membrane Oxygenator

PRINCIPAL INVESTIGATOR: Brack G. Hattler, M.D., Ph.D.  
Federspiel, W. J.; Lund, L. W., Wallace, M.A.  
and Williams, J.L.

CONTRACTING ORGANIZATION: University of Pittsburgh

Pittsburgh, PA 15260

REPORT DATE: June 30, 1995

TYPE OF REPORT: Annual

19960315 102

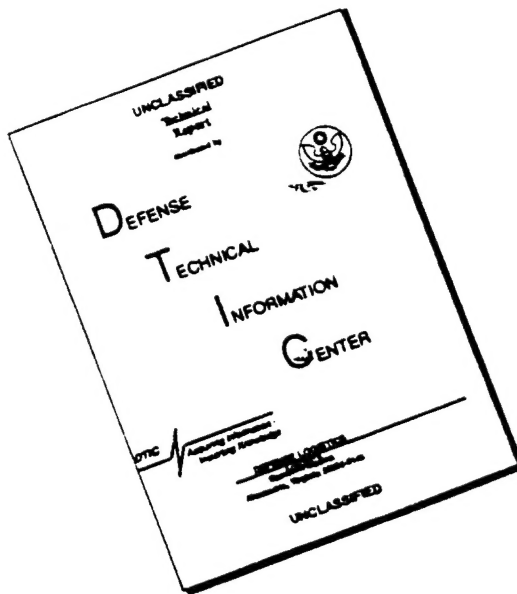
PREPARED FOR: U.S. Army Medical Research and Materiel Command  
Fort Detrick  
Frederick, Maryland 21702-5012

DISTRIBUTION STATEMENT: Approved for public release;  
distribution unlimited

The views, opinions and/or findings contained in this report are  
those of the author(s) and should not be construed as an official  
Department of the Army position, policy or decision unless so  
designated by other documentation.

DTIC QUALITY INSPECTED 1

# **DISCLAIMER NOTICE**



**THIS DOCUMENT IS BEST  
QUALITY AVAILABLE. THE COPY  
FURNISHED TO DTIC CONTAINED  
A SIGNIFICANT NUMBER OF  
PAGES WHICH DO NOT  
REPRODUCE LEGIBLY.**

# REPORT DOCUMENTATION PAGE

Form Approved  
OMB No. 0704-0188

Public reporting burden for this collection of information is estimated to average 1 hour per response, including the time for reviewing instructions, searching existing data sources, gathering and maintaining the data needed, and completing and reviewing the collection of information. Send comments regarding this burden estimate or any other aspect of this collection of information, including suggestions for reducing this burden, to Washington Headquarters Services, Directorate for Information Operations and Reports, 1215 Jefferson Davis Highway, Suite 1204, Arlington, VA 22202-4302, and to the Office of Management and Budget, Paperwork Reduction Project (0704-0188), Washington, DC 20503.

1. AGENCY USE ONLY (Leave blank)			2. REPORT DATE		3. REPORT TYPE AND DATES COVERED		
			June 30, 1995		Annual (1 June 1994 - 30 May 1995)		
4. TITLE AND SUBTITLE			Development of a Novel Intravenous Membrane Oxygenator				
			5. FUNDING NUMBERS				
			DAMD17-94-C-4052				
6. AUTHOR(S)			Brack G. Hattler, M.D., Ph.D.; Federspiel, W.J.; Lund, L.W.; Wallace, M.A.; Williams, J.L.				
7. PERFORMING ORGANIZATION NAME(S) AND ADDRESS(ES)			University of Pittsburgh  Pittsburgh, PA 15260				
			8. PERFORMING ORGANIZATION REPORT NUMBER				
9. SPONSORING/MONITORING AGENCY NAME(S) AND ADDRESS(ES)			U.S. Army Medical Research and Materiel Command Fort Detrick Frederick, MD 21702-5012				
			10. SPONSORING/MONITORING AGENCY REPORT NUMBER				
11. SUPPLEMENTARY NOTES							
12a. DISTRIBUTION/AVAILABILITY STATEMENT			Approved for public release: distribution unlimited.				
			12b. DISTRIBUTION CODE				
13. ABSTRACT (Maximum 200 words)  The Intravenous Membrane Oxygenator (IMO) at the University of Pittsburgh is intended to provide temporary and portable respiratory support to military personnel and civilians whose lungs are acutely impaired. The current IMO device consists of several hundred hollow fiber membranes (HFM's) manifolds to gas supply lines, with a helium-activated pulsating balloon within the fiber bundle for promoting mixing and enhancing gas exchange. This report describes principal progress in the following areas: 1) Development of a simplified test for characterizing gas exchange performance in IMO prototypes. The test shortens the time associated with prototype evaluation, redesign/change, and re-evaluation. 2) Testing and development of IMO Prototype D devices. Limitations to balloon-induced gas exchange enhancement were traced to inefficient pneumatic design of the helium delivery pathway, which is currently undergoing design review and modification. Preliminary modifications to the pathway resulted in significant improvement in balloon dynamics. Additionally, promising pilot work continues on direct mechanical activation of fiber movement to enhance gas exchange. 3) Evaluation of candidate hollow fiber membranes (HFM's). Procedures developed for estimating the gas permeability indicated that some composite HFM's may be unsuitable for IMO application. Other composite HFM's are being investigated, as are silicone coated porous HFM's.							
14. SUBJECT TERMS			Intravenous oxygenator, Artificial lung, Respiratory assist device.				
			15. NUMBER OF PAGES 75				
			16. PRICE CODE				
17. SECURITY CLASSIFICATION OF REPORT		18. SECURITY CLASSIFICATION OF THIS PAGE		19. SECURITY CLASSIFICATION OF ABSTRACT		20. LIMITATION OF ABSTRACT	
Unclassified		Unclassified		Unclassified		Unlimited	

FOREWORD

Opinions, interpretations, conclusions and recommendations are those of the author and are not necessarily endorsed by the US Army.

BT Where copyrighted material is quoted, permission has been obtained to use such material.

PAT Where material from documents designated for limited distribution is quoted, permission has been obtained to use the material.

BAA Citations of commercial organizations and trade names in this report do not constitute an official Department of Army endorsement or approval of the products or services of these organizations.

BAJ In conducting research using animals, the investigator(s) adhered to the "Guide for the Care and Use of Laboratory Animals," prepared by the Committee on Care and Use of Laboratory Animals of the Institute of Laboratory Resources, National Research Council (NIH Publication No. 86-23, Revised 1985).

For the protection of human subjects, the investigator(s) adhered to policies of applicable Federal Law 45 CFR 46.

In conducting research utilizing recombinant DNA technology, the investigator(s) adhered to current guidelines promulgated by the National Institutes of Health.

In the conduct of research utilizing recombinant DNA, the investigator(s) adhered to the NIH Guidelines for Research Involving Recombinant DNA Molecules.

BAA In the conduct of research involving hazardous organisms, the investigator(s) adhered to the CDC-NIH Guide for Biosafety in Microbiological and Biomedical Laboratories.

B. Helms 6/30/95  
\_\_\_\_\_  
PI - Signature Date

## TABLE OF CONTENTS

<b>LIST OF FIGURES . . . . .</b>	iv
<b>LIST OF TABLES . . . . .</b>	vi
<b>1. INTRODUCTION . . . . .</b>	1
<b>1.1 Rationale for an Intravenous Membrane Oxygenator (IMO) . . . . .</b>	1
<b>1.2 Design Goals for the IMO Device . . . . .</b>	4
<b>1.3 Review of Past IMO Prototypes . . . . .</b>	5
<u>Description of Prototypes.</u> . . . . .	5
<u>Comparison among Prototypes</u> . . . . .	7
<b>1.4 Overview of Current Development Approach . . . . .</b>	10
<u>IMO Prototype Characterization</u> . . . . .	10
<u>Fiber Evaluation Studies</u> . . . . .	11
<b>2. BASIC PRINCIPLES OF EXCHANGE IN IMO DEVICES . . . . .</b>	13
<b>2.1 Effective Exchange Permeability of an IMO . . . . .</b>	13
<b>2.2 Fiber Membrane Permeability . . . . .</b>	14
<u>Hollow Fiber Membranes</u> . . . . .	14
<u>Gas Permeability of Hollow Fiber Membranes</u> . . . . .	15
<b>2.3 Liquid Boundary Layer Permeability . . . . .</b>	18
<b>2.4 IMO Exchange Permeability Design Goal . . . . .</b>	19
<b>3. HOLLOW FIBER MEMBRANE EVALUATION AND SELECTION . . . . .</b>	22
<b>3.1 Overview of Fiber Permeability Studies . . . . .</b>	22
<b>3.2 Diffusion Chamber Apparatus and Measurement Procedure . . . . .</b>	23
<b>3.3 Data Analysis . . . . .</b>	26

<i>Calculation of Effective Mass Transfer Coefficient</i> .....	26
<i>Calculation of Membrane Permeability</i> .....	27
<b>3.4 Permeability of MHF 200L Composite Fibers</b> .....	27
<b>3.5 Future Work in Fiber Evaluation</b> .....	28
<b>4. IMO PROTOTYPE DEVELOPMENT</b> .....	32
<b>  4.1 Overview of Characterization Testing</b> .....	32
<i>Rationale for Characterization Testing</i> .....	32
<i>Apparatus and Procedure</i> .....	33
<i>Documentation of Exchange Performance</i> .....	35
<i>Prototype Logging</i> .....	37
<b>  4.2 Exchange Performance of Current Prototypes</b> .....	38
<i>Results of Characterization Testing</i> .....	38
<i>Estimating Exchange Performance in Blood</i> .....	42
<b>  4.3 Analysis of Balloon Pulsation</b> .....	45
<i>Helium Pathway Pneumatics</i> .....	45
<i>Frequency Spectrum of Balloon Pulsation</i> .....	49
<b>  4.4 Gas Flow Dynamics in the IMO</b> .....	53
<i>Rationale for Studies</i> .....	53
<i>Relevant Background Theory</i> .....	54
<i>Experimental Methods</i> .....	54
<i>Pressure and Flow Results in the IMO</i> .....	56
<b>  4.5 Future IMO Prototype Development</b> .....	62
<b>5. CONCLUSIONS</b> .....	65
<b>6. REFERENCES</b> .....	67

## LIST OF FIGURES

<b>Figure 1.1</b> IMO device (Prototype D) as it resides in the inferior vena cava, right atrium, and superior vena cava. . . . .	3
<b>Figure 1.2</b> Schematic of a Prototype D series IMO device showing balloon centrally located around a bundle of parallel hollow fiber membranes. . . . .	6
<b>Figure 1.3</b> Gas exchange performance of a Prototype F series IMO device. . . . .	8
<b>Figure 2.1</b> Relationship between effective (overall) exchange permeability, K, and O <sub>2</sub> exchange rate VO <sub>2</sub> for IMO device in blood. . . . .	20
<b>Figure 3.1</b> Schematic of diffusion chamber apparatus for measuring fiber permeability. . .	24
<b>Figure 3.2</b> CO <sub>2</sub> concentration exiting fiber during washout. . . . .	25
<b>Figure 3.3</b> Overall permeability, K, for O <sub>2</sub> and CO <sub>2</sub> at different stir rates. . . . .	29
<b>Figure 3.4</b> Wilson plot of O <sub>2</sub> and CO <sub>2</sub> permeability measurements at varied stir rates. The intercept is 1/K <sub>m</sub> , the fiber permeability. . . . .	30
<b>Figure 4.1</b> Diagram of mock loop used for <i>in-vitro</i> prototype characterization testing. . . .	34
<b>Figure 4.2</b> Documentation of prototype characterization testing and gas exchange performance. . . . .	36
<b>Figure 4.3</b> O <sub>2</sub> exchange performance of Prototype D01 from characterization testing . . .	39
<b>Figure 4.4</b> O <sub>2</sub> exchange performance of Prototype D02 form characterization testing. . .	40
<b>Figure 4.5</b> Analysis procedure for estimating IMO gas exchange in blood from water characterization testing. . . . .	43
<b>Figure 4.6</b> Estimated exchange performance in blood from characterization testing in water for Prototype D03. . . . .	44
<b>Figure 4.7</b> Pressure and flowrate relationship for helium pathway in Prototype D02. Symbols represent experimental data for air; helium line determined from air regression line. . . . .	47
<b>Figure 4.8</b> Required drive pressure for pulsating 40 ml balloon in Prototype D with existing and with enlarged helium pathways. . . . .	48

<b>Figure 4.9</b> Apparatus for determining frequency spectrum for balloon pulsation in IMO prototypes.	50
<b>Figure 4.10</b> Frequency spectrum of balloon pulsation for IMO prototype D03, with unmodified helium pathway.	51
<b>Figure 4.11</b> Frequency spectrum of balloon pulsation in IMO Prototype D04, with modified helium pathway.	52
<b>Figure 4.12</b> Schematic of pressure-flow apparatus. The air compressor supplies both positive and negative pressure.	55
<b>Figure 4.13</b> The pressure drop versus flow measured in the IMO for air over a relevant range of flow rates. Measurements were done with flow driven by a vacuum and by positive pressure.	57
<b>Figure 4.14</b> Application of compressible Poiseuille flow theory to the pressure-flow data shown in Figure 4.13. In this "compressible" form, pressure drop expressed as pressure-squared drop.	59
<b>Figure 4.15</b> The pressure drop versus flow rate relation measured in the IMO for air and helium flow driven by vacuum pressure. Results are expressed in the incompressible Poiseuille flow form.	60
<b>Figure 4.16</b> The pressure drop versus flow rate relation measured in the IMO for air and helium flow driven by vacuum pressure. Results are expressed in the compressible Poiseuille flow form.	61

## **LIST OF TABLES**

Table 2.1 <i>Hollow Fiber Membranes for IMO Development Work</i> . . . . .	15
Table 4.1 <i>Parameters of Prototypes Used in IMO Development</i> . . . . .	38
Table 4.2 <i>Dimensions of Helium Pathway within IMO Prototype D</i> . . . . .	45

## **1. INTRODUCTION**

This is the annual report for the first year of contract DAMD17-94-C-4052. The report describes progress made over the past year in the ongoing development of an intravenous membrane oxygenator (IMO) in the Artificial Lung Program of the Department of Surgery at the University of Pittsburgh. The University of Pittsburgh IMO device is being designed and developed for the temporary support of soldiers and civilians with acute respiratory failure, whose respiratory systems are unable to maintain adequate gas exchange and who need supplemental support until their lungs return to normal function. For the military, this would include soldiers engaged in chemical warfare with gaseous agents injurious to the lungs. Likewise, as exemplified by the recent terrorist attacks in the subways of Japan, the civilian population is not immune from chemical attack. Although neurotoxic agents were used in the Japanese subway attack, chemicals capable of causing severe pulmonary damage were also available to this terrorist sect. Had they been used, the need for pulmonary support for a large number of civilians would have existed in a setting where the lungs are severely compromised and incapable of adequate gas exchange by traditional ventilator therapy. Accordingly, the availability of a simple device capable of pulmonary support for a large number of potential victims is the military mission for our development of an intravenous membrane oxygenator.

This introductory section of the report presents the rationale and need for an IMO device, highlights the principal design goals for its development, reviews past IMO prototypes leading to the work described here, and summarizes the overall approach of the current development phase.

### **1.1 Rationale for an Intravenous Membrane Oxygenator (IMO)**

Adult respiratory distress syndrome (ARDS) refers to hypoxemic (low arterial PO<sub>2</sub>) respiratory failure arising from a variety of disorders or insults which increase pulmonary capillary permeability, cause pulmonary edema and alveolar flooding, and reduce gas exchange as a result. The general therapeutic action for ARDS sufferers is to support gas exchange while treating the acute event or disease precipitating the ARDS response. These ARDS precipitators can range from pneumonia, shock, trauma, fluid aspiration, and inhalation of smoke and toxic gases, to name just a few. Annually, about 150,000 people within the U.S. suffer from ARDS, and the mortality rate

for adults remains at about 50% (Fazzalari et al, 1994). An intravenous oxygenator would be of great benefit in treating these patients, as well as soldiers who develop ARDS in combat and other military situations.

The preferred method of treatment for people in end-stage ARDS is mechanical ventilation with high inspired O<sub>2</sub> gas concentration. The positive lung airway pressures and excessive volumes associated with ventilation, however, can lead to barotrauma (eg. pneumothorax), volutrauma, and impairment of cardiovascular function (Weinberger, 1992). Furthermore, high O<sub>2</sub> concentration can be toxic to alveolar cells, especially those responsible for surfactant production. Accordingly, even under optimal conditions, mechanical ventilatory support can lead to a worsening of the state of the ARDS lung and the health of the patient. Patients requiring aggressive mechanical ventilatory support can be supported alternatively with extracorporeal oxygenation (ECMO). However application of ECMO is complicated, labor intensive, expensive, and subject to mechanical failure of the pumping system associated with the oxygenator (Fazzalari et al, 1994). Furthermore, the complicated nature of ECMO makes it an unsuitable therapy for emergency application outside of specially trained and equipped centers.

A clear need exists in standard clinical settings, as well as in adverse settings such as combat, for respiratory assistance therapy that is effective, easy to use, portable and economic. The IMO device being developed at the University of Pittsburgh has the potential to provide such a therapy. The device consists of a bundle of hollow fiber membranes which are manifolds to gas supply and removal lines. A pulsating balloon is centrally located within the fiber bundle to provide enhanced fluid mixing. The device is intended to reside in the inferior vena cava, right atrium and superior vena cava, with the membrane fiber axis parallel to the direction of blood flow (Figure 1.1). The device will be inserted at a femoral vein access site with minor surgery or with percutaneous insertion via a facilitating introducer. Once situated within the vena cava, the IMO device will be capable of augmenting gas exchange at the appropriate level even in end-stage ARDS cases. The device will be relatively portable and user-friendly, and hence will not restrict application to specialized hospitals and support staff. Its ultimate suitability for field hospital use means that the IMO device can be an effective respiratory therapeutic for military personnel with ARDS resulting from combat and/or noncombat related insults.

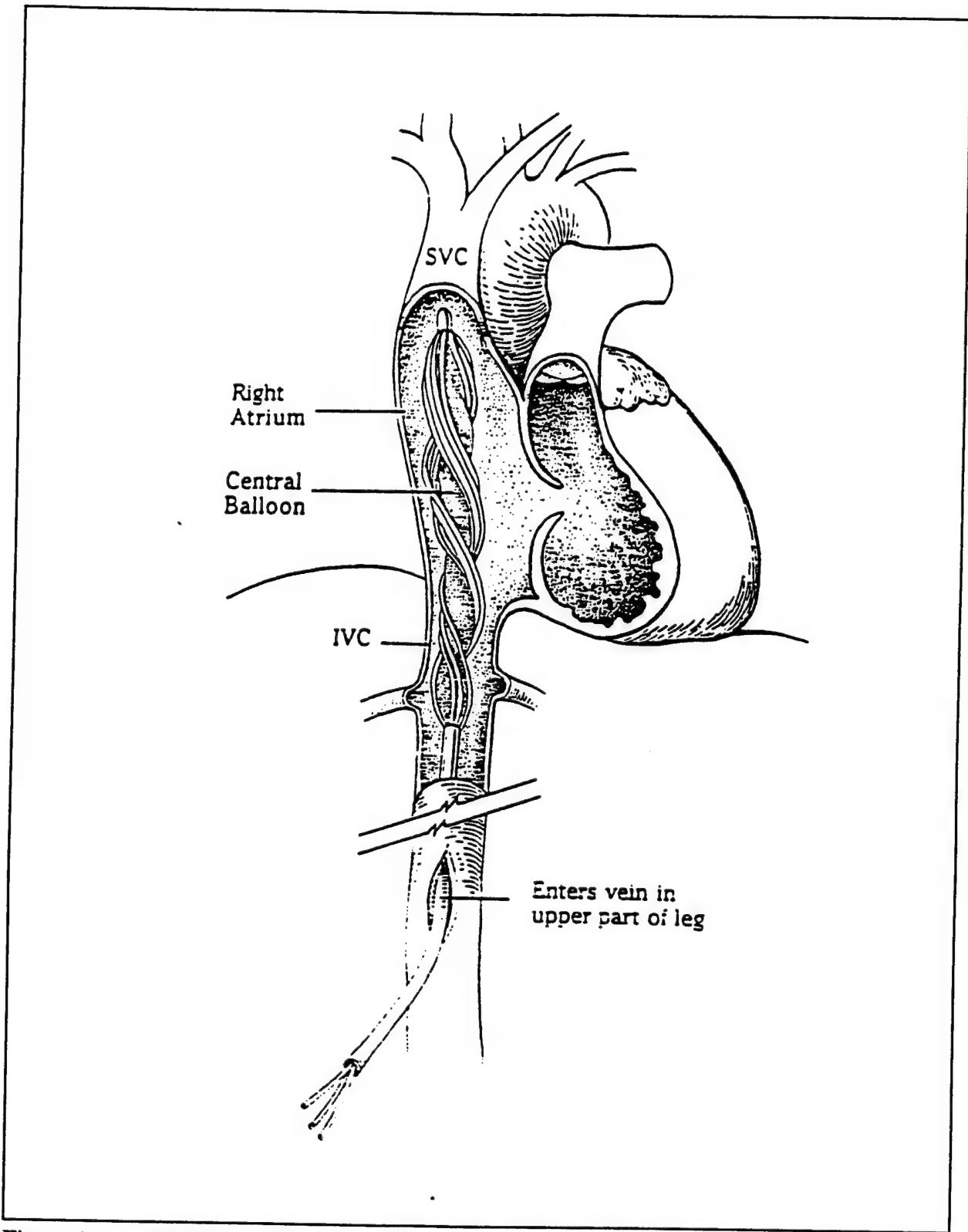


**Figure 1.1** IMO device (Prototype D) as it resides in the inferior vena cava, right atrium, and superior vena cava.

## **1.2 Design Goals for the IMO Device**

The intravenous membrane oxygenator must be able to exchange sufficient oxygen and carbon dioxide to support respiratory function of end stage ARDS sufferers. What that level of exchange is can be difficult to prescribe, but some guidance is provided by recent clinical findings with the IVOX intravascular oxygenator (Conrad et al., 1994). Based on these studies, we have set the target exchange rate goal for the IMO device as one-half the rate of resting O<sub>2</sub> consumption and CO<sub>2</sub> elimination in normal adults. Average resting exchange rates in adults are 270 ml/min for O<sub>2</sub> and 240 ml/min for CO<sub>2</sub> (Grodins and Yamashiro, 1978). *Accordingly, the IMO device must be capable of exchanging 135 ml/min of O<sub>2</sub> and 120 ml/min of CO<sub>2</sub> at normal cardiac outputs in the range of 4-6 L/min.*

The insertion and placement of an IMO device within the vena cava gives rise to pertinent size constraints. The device should be insertable into the vena cava through a pathway originating in the femoral vein. Accordingly, the IMO device must be able to assume a maximum diameter of 1/2" for insertion. Once inserted peripherally and guided into the superior and inferior vena cava, the IMO device must be able to distribute its hollow fiber membranes well across the available cross-section within the vena cava. Thus, our current design allows the fibers of the device to be "unfurled" once the device is in position. The length of the IMO device should be suitable for implantation in a variety of patients. The appropriate length of the device for an adult male is estimated at about 35 cm.

The IMO device must also achieve an adequate gas flow rate for CO<sub>2</sub> removal (1-3 L/min estimated) under a relatively small vacuum pressure, in order to maximize the transmembrane oxygen tension gradient for O<sub>2</sub> transfer. Since the device achieves effective O<sub>2</sub> delivery and CO<sub>2</sub> removal via active mixing of the blood (via the centrally located balloon), hemolysis and biomechanical-induced cellular trauma should be within acceptable limits. We intend to carefully document the hemolysis potential of promising IMO prototypes by exposing them to realistic venous hemodynamics *in vitro* and by implanting them in animals for up to 21 days. Finally, reliability and durability are required of any prototype that is intended for treatment of ARDS, since the required duration of implant may be two to three weeks. In particular, the IMO device

must provide consistent blood oxygenation and carbon dioxide removal while in contact with blood over the intended implant period.

### **1.3 Review of Past IMO Prototypes**

Description of Prototypes. Placing the current development efforts in the proper context requires briefly reviewing past IMO prototypes and the lessons learned from them. Knowledge gained from these earlier prototypes molded our current perspective on developing an intravenous membrane oxygenator. The University of Pittsburgh IMO development program has evolved through six different device configurations, which are designated as Prototypes A through F. Prototypes A, B, and C consist of a bundle of free-floating, narrow hollow fiber membranes which are arranged around a central support rod (or tube). These prototypes differ from one another in the manifolding arrangements for O<sub>2</sub> delivery and CO<sub>2</sub> exhaust. In these and other prototypes, oxygen is aspirated under vacuum pressure through the fibers.

Prototype D is similar to Prototypes A, B, and C in fiber configuration and manifolding, but incorporates a centrally positioned elongated balloon (analogous to the intra-aortic balloon) around which the membrane fibers are bundled (see Figure 1.2; also the IMO depicted in Figure 1.1 represents a Prototype D device). The balloon is rhythmically inflated and deflated using helium gas and a standard Datascope intra-aortic balloon pump console. The balloon pulsations (inflation/deflation) provide a means for active mixing of blood around the fiber membranes, thus enhancing gas (O<sub>2</sub>/CO<sub>2</sub>) exchange.

Prototype E is fabricated from a woven fiber mat, which is rolled concentrically like a "jellyroll" cake and manifolds for oxygen delivery at the distal end and for exhaust at the proximal end. A balloon is placed in the center of the "jellyroll" and inflated rhythmically. The long axis of the membrane fibers is again parallel to the direction of blood flow. Different E series prototypes differ from one another in the configuration of the distal tip and thus the manner in which blood is permitted to flow through the "jellyroll" device.

Prototype F is similar in appearance to a scroll and is fashioned as a mat from hollow fiber membranes that are arranged with the fiber axis *perpendicular* to the flow of blood. This orientation allows cross-flow of blood past the fibers, a flow pattern which engenders appreciably

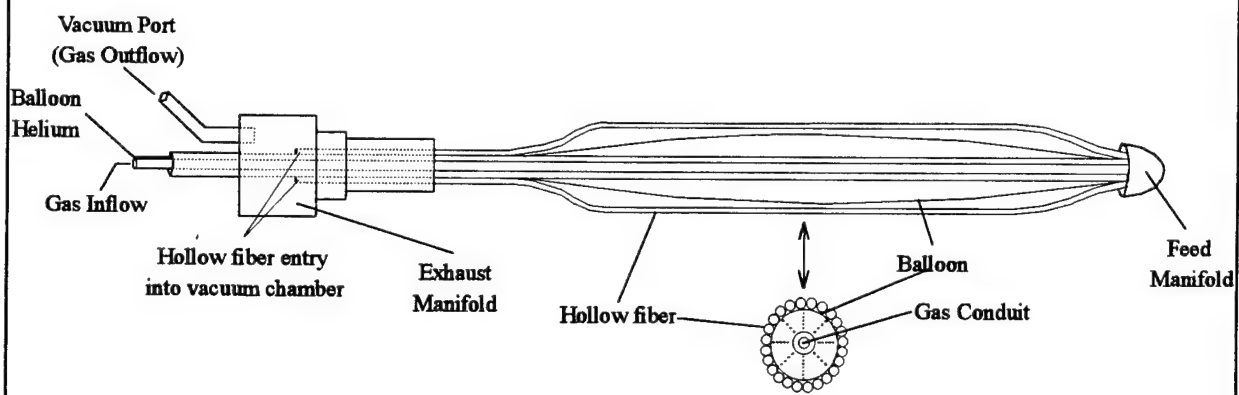


**Figure 1.2** Schematic of a Prototype D series IMO device showing balloon centrally located around a bundle of parallel hollow fiber membranes.

better mass transfer than parallel blood flow. Oxygen is introduced through a longitudinal tube along one side of the woven mat, and is vacuumed from a second longitudinal tube that receives the opposite end of each hollow fiber in the mat. Oxygen enters the delivery tube and is distributed horizontally through the fibers which connect to the vacuum port where unused oxygen and the carbon dioxide removed from the blood are exhausted. This configuration allows for short gas flow paths regardless of the length of the device, which is a useful design consideration for effective vena caval oxygenation. A centrally placed balloon enhances convective mixing of the blood while also moving the membrane sheets within the scroll arrangement. The scroll itself can be tightly wrapped around the balloon for insertion, and then unfurled once in position within the venous system.

Comparison among Prototypes. The different early prototypes were tested for gas ( $O_2/CO_2$ ) exchange using physiologic saline as a standard for comparison between different device configurations, and to establish optimum operational parameters for subsequent examination with abattoir ox blood. In our initial Prototypes A-C, the hollow fiber membranes were free floating and arranged parallel to the direction of blood flow. These devices contained no mechanism for active mixing or movement of the fibers. Gas exchange performance of these devices was inconsistent and led us to introduce a centrally positioned balloon as a means for enhancing convective mixing of the blood around the hollow fiber membranes. Oxygen and carbon dioxide transfer demonstrated a positive dependence on balloon pulsation frequency for all balloon-incorporating prototypes, with marked improvement over gas transfer rates measured for the static fiber configuration.

The best gas exchange performance in past IMO prototypes occurred for a Prototype F series device. Results are shown in Figure 1.3 as area normalized  $O_2$  exchange rate in blood as a function of balloon pulsation frequency. This F series prototype exhibited an appreciable increase in achievable rates of area-normalized oxygen transfer compared to earlier prototype designs, with a maximum normalized rate of about 200 ml/min/m<sup>2</sup>. Comparatively, the maximum normalized  $O_2$  exchange rate was 150 ml/min/m<sup>2</sup> in Prototype D series and 170 ml/min/m<sup>2</sup> in Prototype E series. Generally, although gas exchange performance improved with active mixing, it varied significantly among identical prototypes. Furthermore, all prototypes exhibited behavior

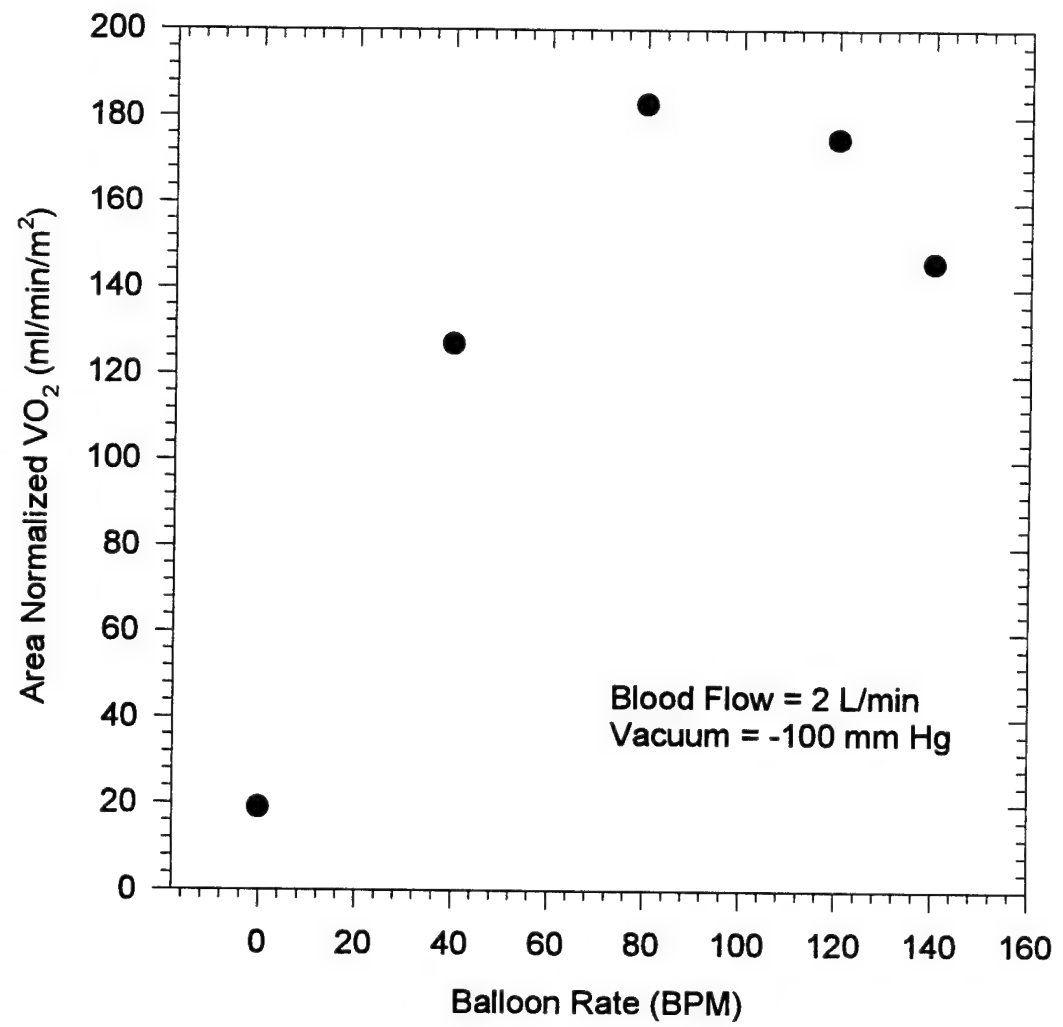


**Figure 1.3** Gas exchange performance of a Prototype F series IMO device.

similar to that shown in Figure 1.3, in which a clear limit to balloon augmented exchange is seen.

Figure 1.3 suggests that a scaled up Prototype F device with fiber area between 0.5 and 0.7 m<sup>2</sup> would be capable of sufficient gas exchange to meet our exchange rate design goal. The subsequent development efforts aimed at scaling up Prototype F devices, however, were unsuccessful. The denser fiber mats which were used in Prototype F presented a substantial resistance to blood flow through the device, and the resulting pressure drops were too large to be compatible with the venous circulation. Furthermore, the hemolysis associated with blood flow through the dense mat was also unacceptably high. Finally, the denser fiber mats of scaled up Prototype F devices would ultimately present substantial difficulties with insertion through a peripheral venous access site.

*Accordingly, current IMO development efforts have shifted focus back to the simpler Prototype D device, which presents a markedly smaller resistance to blood flow per fiber area compared to other prototypes, and which configures more easily to the maximum size constraint consistent with peripheral venous insertion.* The incorporation of a pulsating balloon, which generates three-dimensional convective mixing of the blood flow around the hollow fibers (as confirmed by earlier laser-based flow visualization studies, see Hattler et al, 1992), distinguishes our IMO prototype design from those of others. Nevertheless, successful development of a Prototype D device requires strict optimization of the augmentation of gas exchange associated with balloon pulsation. Our past development work has demonstrated the benefit of balloon pulsation, but we have yet to realize its full potential. The principal resistance to exchange in fiber oxygenators is associated with imperfect mixing in the blood phase subjacent to the fibers (see Section 2). In principle then, increasing the intensity of balloon pulsation will increase mixing and improve exchange rate (up to a limit imposed by the fiber permeability, which would be an exchange rate appreciably above our design goal).

Our past development work, however, has always seen a clear limit to the augmentation of gas exchange associated with balloon pulsation. Our past prototypes have all shown behavior similar to that shown in Figure 1.3, in which a maximum augmentation of exchange is seen at a balloon rate of about 80 bpm. The current development work focuses on identifying and eliminating those factors which limit the augmentation of gas exchange by balloon pulsation within

our IMO device. *We believe that a D series prototype IMO device with optimized balloon pulsation and exchange augmentation will allow us to achieve the requisite O<sub>2</sub>/CO<sub>2</sub> exchange for effective treatment of ARDS.*

#### **1.4 Overview of Current Development Approach**

The current developmental approach has been designed to facilitate prototype design changes and expedite device evaluation and evolution. The approach consists of two separate but obviously interrelated thrusts: characterization studies of complete IMO prototypes, and evaluation studies of candidate hollow fiber membranes.

*IMO Prototype Characterization.* The characterization studies of complete IMO prototypes have been streamlined to facilitate rapid design evaluation and evolution. A Prototype Development Characterization Test (PDCT) has been designed and incorporated in which prototypes undergo standard evaluation in an *in-vitro* circulation loop using water as the working fluid. The PDCT allows for valid and expedient comparisons to be made among IMO prototypes as design changes are incorporated. Furthermore, the simplified PDCT has shortened the time associated with the iterative loop between design evaluation, design change/adjustment, and design re-evaluation. Accordingly, developmental progress toward our design goals can be realized more rapidly than if all prototypes were subjected to complete blood and *in-vivo* testing at this juncture in the developmental process. In addition, the process is more economical in that prototypes which undergo water testing are available for further design modification and re-evaluation.

As an available part of the PDCT, an engineering dimensionless analysis is used to estimate exchange performance in blood under physiological flow conditions from the *in-vitro* water characterization tests. This procedure has been carefully evaluated by Vaslef et al (1994a, 1994b) in studies on extracorporeal and intracorporeal artificial lungs simultaneously tested in both water and in blood. The ability to estimate exchange performance in blood is important because a given prototype exchanges more gas with blood than with water. Thus, although PDCT involves water testing, the data analysis allows assessing prototype performance vis-a-vis our ultimate design goal for exchange in blood.

We plan to do the simplified PDCT in conjunction with design development until an IMO

device is available which performs within 75% of our design goal for exchange in blood (based on the estimating analysis described above). These candidate IMO devices will then undergo further, more elaborate characterization testing as outlined within the original proposal. These more elaborate characterization tests will involve 1) *in-vitro* testing with blood, looking at gas exchange, flow resistance, and hemolysis generation; and 2) *ex-vivo* and *in-vivo* implants in adult male sheep. The animal studies will assess gas exchange, device biocompatibility, venous hemodynamics, end-organ anatomy and physiology, and device implant durability. *Thus, our overall development procedure reserves animal experiments for only those IMO devices with demonstrated exchange performance relative to the requisite exchange goal for O<sub>2</sub> and CO<sub>2</sub>.*

**Fiber Evaluation Studies.** A separate set of studies addresses the evaluation and selection of an appropriate hollow fiber membrane for the IMO device. Candidate fibers are tested in a diffusion chamber apparatus which allows determination of fiber exchange permeability. There are numerous commercially available hollow fiber membranes which are suitable for oxygenator devices. The goal of the fiber evaluation studies is to measure the exchange permeability of available fibers to aid selection of an IMO candidate fiber with appropriate exchange permeability. In particular, we are interested in evaluating composite hollow fiber membranes, which have a nonporous (true membrane) polymer layer within their porous walls. Composite hollow fiber membranes are ideal candidates for IMO devices because the true membrane blocks fluid infiltration, wetting of the fiber, and associated degradation of exchange performance. The nonporous polymer layer, however, reduces fiber permeability considerably compared to porous fibers. Accordingly, determining the permeability of these and other hollow fiber membranes becomes critical to overall IMO development. Ultimately, as balloon pulsation improves mixing within the IMO device, and transport resistance within the blood phase diminishes, fiber permeability could potentially limit exchange unless a suitable fiber is selected.

The fiber permeability studies done in the diffusion chamber also allow separate investigations of other fiber related issues critical to IMO development. These include, for example, controlled studies of 1) fiber wetting and degradation in porous and composite hollow fiber membranes; 2) interaction of blood with the hollow fiber polymer membrane; 3) and the effect of antithrombotic coatings on exchange permeability of fibers. Studying these and other

issues using complete IMO prototypes would lengthen the development time associated with fiber evaluation and selection.

## 2. BASIC PRINCIPLES OF EXCHANGE IN IMO DEVICES

This section briefly presents the theoretical background relevant to gas exchange in IMO devices. This background will be useful to the discussions in subsequent sections concerning IMO device performance, and evaluation of candidate hollow fiber membranes. Most importantly, the concept of an effective exchange permeability for an IMO device is introduced and is related to its principal underlying determinants: the fiber membrane permeability and the liquid-side (blood-side) boundary layer permeability. The effective gas exchange permeability of an IMO device represents a mass transport coefficient for overall gas exchange. As such, it provides a useful gauge for evaluating the efficiency of gas exchange associated with the device, and for interpreting performance and evaluating progress during IMO device development.

### 2.1 Effective Exchange Permeability of an IMO

The effective or overall exchange permeability, K, of an IMO device represents the rate of gas exchange normalized to fiber surface area and to the gas partial pressure differences driving exchange. Focusing on O<sub>2</sub> as the species of interest, the overall IMO device O<sub>2</sub> exchange rate, VO<sub>2</sub>, is given by

$$VO_2 = K A (\bar{P}_g - \bar{P}_l) \quad (2.1)$$

where  $\bar{P}_g$  and  $\bar{P}_l$  are the *average* O<sub>2</sub> partial pressures<sup>1</sup> in the gas and liquid (blood) phases, respectively, and A is the fiber membrane surface area. A similar relationship can be written to define the effective exchange permeability of the device for CO<sub>2</sub>. The effective exchange permeability of an IMO device represents a useful parameter for interpreting results because it most closely reflects transport *diffusional resistance* to gas exchange, with permeability and resistance being inversely related. Accordingly, permeability provides a measure of the relative

---

<sup>1</sup> Relating the average partial pressures in the blood or gas phases to the blood and gas inlet and outlet partial pressures goes beyond the scope of this summary. Nevertheless, a simple arithmetic average of inlet and outlet partial pressures often provides a useful estimate of exchange performance in an IMO device.

efficiency of gas exchange of an IMO device, independent of other issues such as convective flow.

In general, because of imperfect convective mixing within blood and gas phases, exchange involves diffusion not only through the fiber wall, but through the gas and blood phases as well. The diffusion coefficient within the gas phase is relatively large, however, and so transport resistance there can generally be neglected. Accordingly, the overall permeability of an IMO device has two principal determinants

$$\frac{1}{K} = \frac{1}{K_m} + \frac{1}{K_l} \quad (2.2)$$

where  $K_m$ , and  $K_l$  represent the individual permeabilities of the fiber membrane and liquid (blood) phases, respectively. The reciprocal relation arises because the individual contributions represent resistances in series, which add directly to determine overall resistance. One implication of the relationship above is that the overall permeability,  $K$ , is always less than the smallest of the permeabilities,  $K_m$ , and  $K_l$ . In simple terms, the transport process with the smallest permeability controls gas exchange in the overall device. Thus, development efforts should always focus principally on increasing the smallest permeability associated with the device.

## 2.2 Fiber Membrane Permeability

*Hollow Fiber Membranes.* Hollow fiber membranes (HFs) can be categorized according to different wall morphologies. Porous fiber membranes are the most common HFs used for oxygenator design. The porous HFs have fixed submicron pores within the wall that are contiguous from outer to inner lumen. Accordingly, the polymer material generally does not determine exchange performance and behavior as much as the pore size and characteristics. The key parameters in this regard are the mean pore size,  $d_p$ , and the wall porosity,  $\epsilon$ , which represents the fractional wall volume consisting of pores. One important polymer-related fiber property is the fiber's hydrophobic versus hydrophilic nature. Generally, hydrophobic fibers are used in oxygenators because they resist fluid wetting under normal transmural pressure differences. As will be elucidated below, fiber wetting can markedly reduce the exchange permeability of the fiber.

The remaining classes of hollow fiber membranes are the nonporous fibers and the composite fibers. The nonporous HFMs have walls consisting of a homogeneous, poreless polymer. These fibers are often referred to as "true" membranes because they provide absolute separation (or segregation) of the liquid and gas phases. A true membrane fiber with walls thick enough for structural support would have a relatively low gas permeability relative to a porous fiber. Accordingly, composite fibers combine a thin true membrane for liquid and gas segregation within a porous wall for mechanical support and optimal gas permeability. To the best of our knowledge, Mitsubishi manufactures the only commercially available composite fibers (Mitsubishi MHF fibers). However, we have recently identified another Japanese company (Kuraray) which may be also supply a composite fiber membrane.

Table 2.1 lists some of the hollow fiber membranes available commercially for IMO development work. All fibers listed are polypropylene hydrophobic fibers. The table provides fiber internal lumen size, wall thickness, wall porosity, and pore size (where available). The gas permeability of hollow fiber membranes is discussed in the following section.

*Table 2.1 Hollow Fiber Membranes for IMO Development Work*

	inner diameter $d_i$ ( $\mu\text{m}$ )	wall thickness $h$ ( $\mu\text{m}$ )	wall porosity $\epsilon$ ( $\mu\text{m}$ )	pore size $d_p$ ( $\mu\text{m}$ )
Celgard x10 <sup>a</sup>	200	30	30	.05
Celgard x20 <sup>a</sup>	200	30	40	.07
KPF 190M <sup>b</sup>	200	22	45	
MHF 200L <sup>c</sup>	200	27	41	

a - Hoechst Celanese, also available in 240 and 400 micron inner diameters

b,c- Mitsubishi Rayon

c- a composite fiber with a 1  $\mu\text{m}$  polyetherurethane membrane in middle of wall

**Gas Permeability of Hollow Fiber Membranes.** Predicting the exchange capacity of a particular HFM requires knowing the permeability,  $K_m$ , of the fiber membrane. This value is not

usually available, however, in the specifications provided by the fiber manufacturer. Indeed  $K_m$  values can be difficult to determine experimentally for several reasons. If  $K_m$  is measured in a system with gas on one side of the membrane and liquid on the other, the measurement is easily affected by unmixed liquid boundary layers adjacent to the surface of the fiber wall. These unmixed boundary layers present an additional resistance to diffusion, and hence reduce the effective permeability measured. If  $K_m$  is measured in a system with gas on both sides of the membrane, bulk gas flow can occur through the walls of porous fibers if total pressure is not the same on both sides of the membrane. Thus, the measured permeability may be appreciably larger than if a liquid were on one side of the membrane, as in the actual case for the IMO device.

For porous hollow fiber membranes, values of  $K_m$  can be estimated from basic diffusion theory (Hines and Maddox, 1985) assuming the pores within the wall remain gas filled. The appropriate relationship is given by

$$K_m = \frac{\epsilon D}{\tau \delta P_0} \quad (2.3)$$

where all parameters have been previously defined except for  $D$ , the gas diffusion coefficient in the pores,  $P_0$ , standard atmospheric pressure, and  $\tau$ , a tortuosity factor accounting for a gas diffusional pathway which is longer than the membrane thickness. As example, assuming a wall porosity of  $\epsilon=0.45$  and thickness of  $\delta=22$  microns, as in the Mitsubishi KPF porous fiber (Table 2.1), a diffusion coefficient for  $O_2$  of  $D = 7.5 \times 10^{-2}$  cm $^2$ /s for Knudsen pore diffusion of  $O_2$  at 37°C (Hines and Maddox, 1985), and a tortuosity factor of  $\tau=3$  (Qi and Cussler, 1985), the computed fiber permeability is  $K_m = 6 \times 10^{-2}$  ml  $O_2$ /cm $^2$ /s/cmHg. This theoretically estimated value is close to the experimentally measured value of  $6.7 \times 10^{-2}$  ml  $O_2$ /cm $^2$ /s/cmHg reported by Kamo *et al.* (1990) for the Mitsubishi KPF fiber in gas-membrane-gas system.

A permeability value of  $K_m \sim 10^{-2}$  ml  $O_2$ /cm $^2$ /s/cmHg for porous HFM represents an enormous  $O_2$  exchange capacity which is never realized in an oxygenator device. Putting this value in perspective, an IMO device with 0.5 m $^2$  surface area of these fibers, and with an average 70 cmHg  $PO_2$  difference between the gas and blood phases, could potentially exchange 210 L/min

of O<sub>2</sub>! This exchange rate, of course, is several thousand fold greater than actually occurs because substantial resistance to exchange resides within the blood phase, in small imperfectly mixed boundary layers adjacent to the fiber wall surfaces. Hence, the overall effective exchange permeability within an IMO device is substantially less than the permeability of the individual porous HFMs composing the device.

Liquid infiltration into gas filled pores can markedly diminish the exchange performance of an HFM. Even with hydrophobic HFMs, evidence suggests that the pores do not remain completely gas filled, but that liquid does penetrate into the fiber wall (Qi and Cussler, 1985). For entirely liquid filled pores, the fiber membrane permeability is markedly reduced because the diffusion coefficient for O<sub>2</sub> in water is about  $2 \times 10^{-5}$  cm<sup>2</sup>/s, substantially less than that in gas, and because the capacity (or solubility) of O<sub>2</sub> in a liquid is small. For the same pore tortuosity and membrane thickness as in the previous example, appropriate theory for O<sub>2</sub> diffusion through water filled pores estimates a fiber permeability of  $K_m \sim 3 \times 10^{-7}$  ml O<sub>2</sub>/cm<sup>2</sup>/s/cmHg, a reduction in exchange capacity of nearly 5 orders of magnitude compared to a dry fiber wall. Thus, there is a clear benefit to using hydrophobic HFMs with nonwetting properties in an IMO device. Even so, Qi and Cussler (1985) measured  $K_m$  for the Celgard X20, a polypropylene hydrophobic porous HFM, and concluded that the situation rests somewhere between gas-filled and liquid-filled pores. Their measured  $K_m$  value (converted to units used here) was  $K_m \sim 2 \times 10^{-4}$  ml O<sub>2</sub>/cm<sup>2</sup>/s/cmHg.

The permeability of a composite HFM is markedly affected by the characteristics of the true membrane used within the porous fiber wall. In general, homogeneous polymer films have low gas permeabilities. Permeation of a gas species across nonporous polymers involves absorption of gas molecules on the polymer surface, diffusion through the polymer molecular matrix, and desorption of the gas species at the opposite surface. Kamo *et al.* (1990) measured the membrane permeabilities of the Mitsubishi composite HFMs. The MHF M series incorporates a 1/2 micron polyurethane true membrane and had  $K_m = 1.6 \times 10^{-5}$  ml O<sub>2</sub>/cm<sup>2</sup>/s/cmHg. The MHF L series, with a 1 micron polyurethane true membrane, had  $K_m = 0.9 \times 10^{-6}$  ml O<sub>2</sub>/cm<sup>2</sup>/s/cmHg. These permeabilities are markedly smaller than those applicable to porous HFMs and indicate that the true membrane component of composite HFMs dictate the overall exchange permeability of the fiber.

### 2.3 Liquid Boundary Layer Permeability

The liquid (blood) phase permeability,  $K_l$ , accounts for diffusion from the fiber surface through the imperfectly mixed liquid boundary layers which arise adjacent to the fiber surfaces. Even a relatively small (micron size) unmixed liquid layer can reduce  $K_l$  appreciably below the fiber  $K_m$ , and limit overall exchange. Furthermore, generating convective mixing on the scale of microns subjacent to a surface is difficult, and so diffusional boundary layers will always be present and will impact upon exchange. For simple liquids like water, the permeability of a liquid boundary layer of thickness  $\delta_{bl}$  can be expressed as

$$K_l = \frac{\alpha D}{\delta_{bl}} \quad (2.4)$$

where  $\alpha$  and D are the gas solubility and diffusion coefficient in the liquid. The liquid boundary layer thickness,  $\delta_{bl}$ , can be considered an average distance that the gas must diffuse away from the fiber before being swept out of the IMO device by the bulk flow of liquid. Accordingly, the value of  $\delta_{bl}$  depends principally on the flow dynamics in the liquid phase, which is complicated in the IMO device. The principal role of balloon pulsation in the IMO device is to maximize convective mixing within the blood phase so that the diffusional boundary layer thickness is minimized, and the permeability maximized.

Generally, the permeability of the liquid boundary dominates (limits) exchange in oxygenator devices. For example, the  $K_l$  value for  $O_2$  diffusing through a water boundary layer of 1 micron in thickness is about  $9 \times 10^{-5}$  ml  $O_2/cm^2/s/cmHg$ . Assuming a hydrophobic porous fiber, the value for  $K_m$  is in the range of  $10^{-2}$  to  $10^{-4}$  ml  $O_2/cm^2/s/cmHg$ , provided the fiber is not completely wetted. Accordingly, a liquid boundary layer of 1 micron, just a fraction of the fiber size, has an  $O_2$  permeability appreciably below that of the fiber membrane, or  $K_l \ll K_m$ . Under these conditions, the overall IMO gas exchange permeability would be dictated by the liquid boundary layer, and

$$K \approx K_l \quad (2.5)$$

Only under conditions of markedly reduced  $K_m$ , as would accompany for example complete fiber wetting, would the permeability of a porous HFM have an appreciable influence on IMO exchange performance. Nevertheless, we include  $K_m$  in the overall exchange relation, Eq. 2.2, as a reminder that fiber permeability can potentially affect exchange performance. The permeability of composite hollow fiber membranes is reduced by the presence of the true membrane and may become comparable to that of the liquid boundary layer. For example, the permeability of the Mitsubishi composite fiber falls in the range of  $10^{-5}$  to  $10^{-6}$  ml O<sub>2</sub>/cm<sup>2</sup>/s/cmHg. As a result, the overall exchange rate in an IMO device utilizing these composite fibers can potentially be affected by the permeability of the fibers themselves. These issues are important to the IMO development process and will be discussed further when results from fiber permeability studies are presented in Section 3 of this report.

## 2.4 IMO Exchange Permeability Design Goal

The design goal for O<sub>2</sub> exchange rate in an IMO can also be expressed as the required effective permeability, K, of a device accomplishing the desired exchange. This involves rearranging Eq. 2.1, and for a given VO<sub>2</sub>, estimating the mean O<sub>2</sub> partial pressures within the gas and blood phases under typical operation. The mean O<sub>2</sub> partial pressure within the gas phase is relatively simple to estimate. Gas enters the IMO device at 100% O<sub>2</sub> and leaves with only minor dilution by CO<sub>2</sub>. Assuming that gas flows under a vacuum pressure of 25 cmHg relative to atmospheric pressure (P<sub>0</sub>=76 cmHg), the mean O<sub>2</sub> gas tension within the gas phase would be about 62 cmHg. Estimating the mean O<sub>2</sub> partial pressure in the blood phase requires specifying the blood flow rate, the inlet blood PO<sub>2</sub> (venous PO<sub>2</sub>), and the relationship between blood O<sub>2</sub> content and partial pressure (i.e. the blood O<sub>2</sub> capacity curve, which accounts for the oxygen carrying capacity of hemoglobin and for dissolved oxygen; see Reeder, 1986). Thus, for a given O<sub>2</sub> exchange rate and blood flowrate, the change in O<sub>2</sub> content of blood can be computed. Then, using the inlet (or venous) PO<sub>2</sub> and the blood O<sub>2</sub> capacity curve, the outlet (or arterial) PO<sub>2</sub> can be computed and used to determine the mean blood O<sub>2</sub> partial pressure required for Eq. 2.1.

The relationship between the effective permeability, K, of an IMO device and the resulting O<sub>2</sub> exchange rate, VO<sub>2</sub>, is shown in Figure 2.1. The blood parameters used in Figure 2.1

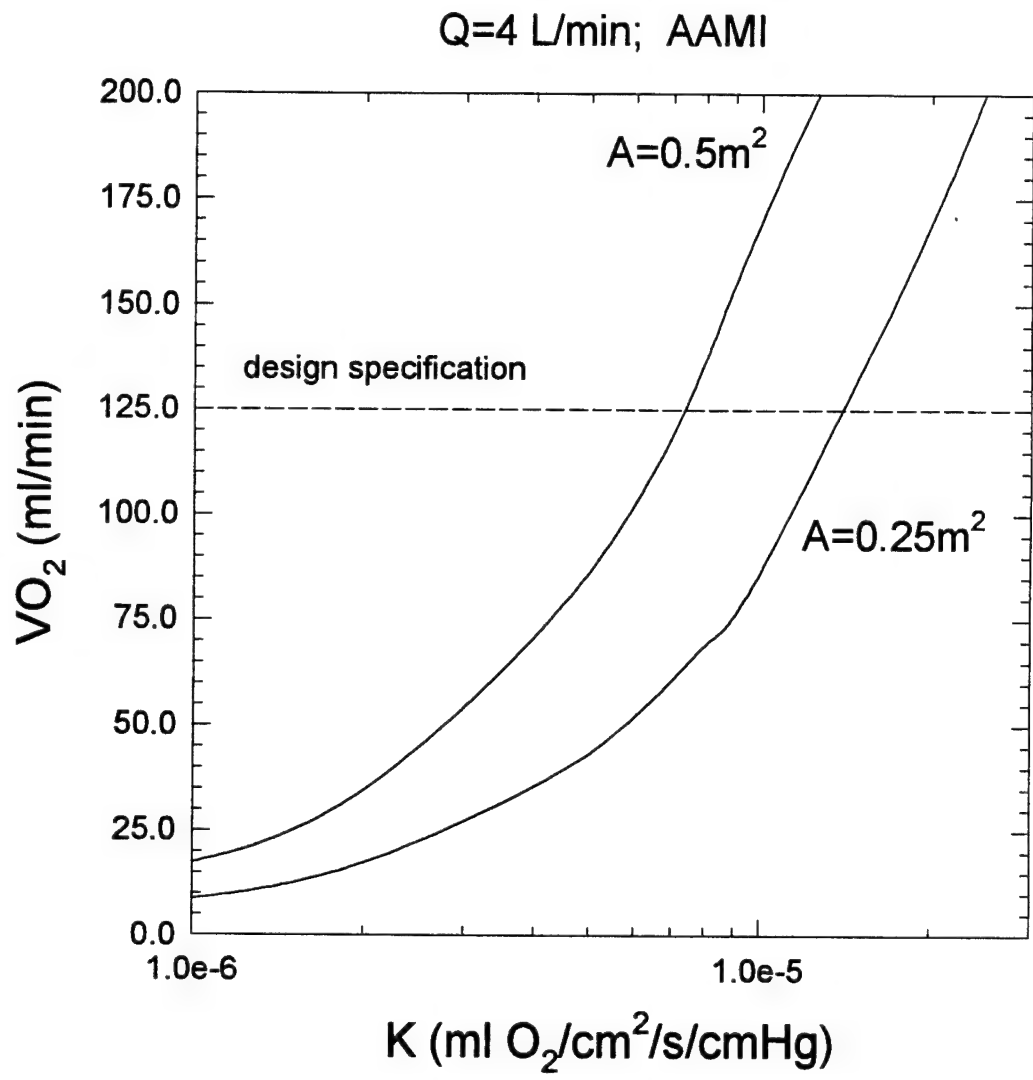


**Figure 2.1** Relationship between effective (overall) exchange permeability,  $K$ , and  $O_2$  exchange rate  $VO_2$  for IMO device in blood.

correspond to standard AAMI conditions for testing blood oxygenators, with a blood flow of 4 L/min and an inlet blood PO<sub>2</sub> of 40 mmHg. Relationships are shown for IMO devices with total fiber surface areas, A, of 0.5m<sup>2</sup> and 0.25m<sup>2</sup>, and the level of oxygen exchange corresponding to our design goal is indicated. Accordingly, this analysis indicates that an IMO device with fiber area in the range indicated requires an overall exchange permeability, K, in the range:

$$7 \times 10^{-6} \text{ ml O}_2/\text{cm}^2/\text{s}/\text{cmHg} < K < 1.5 \times 10^{-5} \text{ ml O}_2/\text{cm}^2/\text{s}/\text{cmHg}$$

This permeability range provides an alternative gauge, in addition to VO<sub>2</sub> and the area normalized VO<sub>2</sub>, for assessing progress during the IMO development phase.

The effective permeability required of our IMO device can be compared to effective permeabilities of commercial extracorporeal oxygenators. Although not normally available from manufacturers, the overall permeability of extracorporeal oxygenators can be computed, much as described for the IMO device, from information provided in several manufacturer's performance specifications. In the same units reported above, the effective permeability of the Bentley Univox is estimated at  $3-4 \times 10^{-6}$ , compared to  $1-2 \times 10^{-6}$  for the Avecor Ultrox, and  $5-6 \times 10^{-6}$  for the Sarns Turbo. Thus, the design goal for the IMO device requires developing an oxygenator which is roughly 2-4 times more efficient in O<sub>2</sub> exchange than extracorporeal oxygenators, which can compensate for smaller exchange efficiency by using larger exchange surface area. *Ultimately, the IMO device will achieve more efficient O<sub>2</sub> exchange than extracorporeal oxygenators by optimizing the active convective mixing engendered by balloon pulsations.*

### **3. HOLLOW FIBER MEMBRANE EVALUATION AND SELECTION**

This section describes the apparatus and methodology used to measure hollow fiber membrane (HFM) permeability. The evaluation of the HFMs is necessary to isolate their effect on overall IMO permeability, and to provide a means for ultimate selection of the HFM most appropriate for the IMO. In addition, by knowing the HFM permeability, the maximum mass transfer capacity of the IMO is defined. The procedure for performing these evaluations was designed with the goal of providing accurate and repeatable results in a simple, inexpensive and rapid manner. The procedure has been used to make preliminary permeability measurements of the commercially available Mitsubishi MHF fibers. The results have helped define the characteristics of an optimal fiber for intravenous membrane oxygenation.

#### **3.1 Overview of Fiber Permeability Studies**

The purpose of performing fiber permeability studies is not only to quantify fiber permeability but also to provide a means for comparing various hollow fiber membrane types. These studies will allow comparisons to be made with respect to both oxygen and carbon dioxide fiber permeability as well as studies of the long term effects on permeability of fiber exposure to liquid (water, plasma, blood). Hollow fiber membranes are either of a microporous or composite nature (see Section 2). Microporous membranes comprised of hydrophobic material typically manifest greater permeabilities, but due to wetting and serum leakage, these permeabilities may degrade over time. Composite membranes consist of combined microporous and true membrane layers which prevent fluid infiltration. Properly constructed composite membranes may allow sufficiently high permeabilities which will be maintained over extended periods of time due to the nature of the true membrane layer.

The hollow fiber membranes in the IMO will be immersed in blood for up to three weeks. Accordingly, permeability measurements should be made in a gas-liquid environment. Permeability measured in a gas-gas system would be affected by bulk flow through the microporous fiber wall. Additionally, gas-gas measurements would fail to reflect the interactions of the fluid with the membrane. In a gas-liquid system, however, a liquid diffusional boundary layer at the outer surface of the fibers presents additional resistance to mass transfer, and reduces

permeability. It is therefore necessary to account for this effect so that the actual membrane permeability can be determined from the system permeability measurements. A diffusion chamber has been designed and constructed to perform these studies. The measurement procedure and data analysis methodology are described below.

### **3.2 Diffusion Chamber Apparatus and Measurement Procedure**

The diffusion chamber is based on a closed volume, time dependent (batch) mass transfer process, as opposed to a flow through steady-state system. This arrangement allows for a simpler design as well as a simpler permeability measurement protocol. The chamber consists of a parallel arrangement of fibers submerged in a stirred liquid bath of fixed volume (300 cc). Gas is drawn through the lumen of the fibers using a vacuum pump at regulated flow rates. Additional features include a heat exchanger which allows for measurements to be made at 37°C, compliance balloons to allow for removal of sample volumes, and sealed ports for insertion of a temperature probe as well as on-line oxyhemoglobin saturation measurements. The components of the diffusion chamber measurement procedure are depicted in Figure 3.1.

Fiber permeability is currently determined by measuring the change in effluent gas species concentrations over time with a mass spectrometer (Medical Gas Analyzer, Marquette Electronics, Milwaukee, WI). Gas side measurements provide greater accuracy compared to liquid side measurements. The liquid bath is initially equilibrated with high concentrations of oxygen or carbon dioxide, at which time the fiber gas source is switched to nitrogen, such that the fiber inlet O<sub>2</sub> or CO<sub>2</sub> concentration is zero. The outlet O<sub>2</sub> or CO<sub>2</sub> content is measured by the mass spectrometer and recorded on a personal computer with an A/D board. The rate of the exponential washout of O<sub>2</sub> or CO<sub>2</sub> is determined from these measurements and used to calculate the permeability of the fiber-liquid system, as will be discussed below. Figure 3.2 shows a sample set of data for CO<sub>2</sub> transfer plotted on a natural log scale versus time. A linear regression curve is plotted through the data series to determine the slope which is in turn used to calculate permeability. By making these measurements at different stir rates, the actual membrane permeability can be estimated by extrapolating the measured mass transfer coefficients to infinite stirring rates where the resistance to mass transfer is due solely to the fiber membrane.

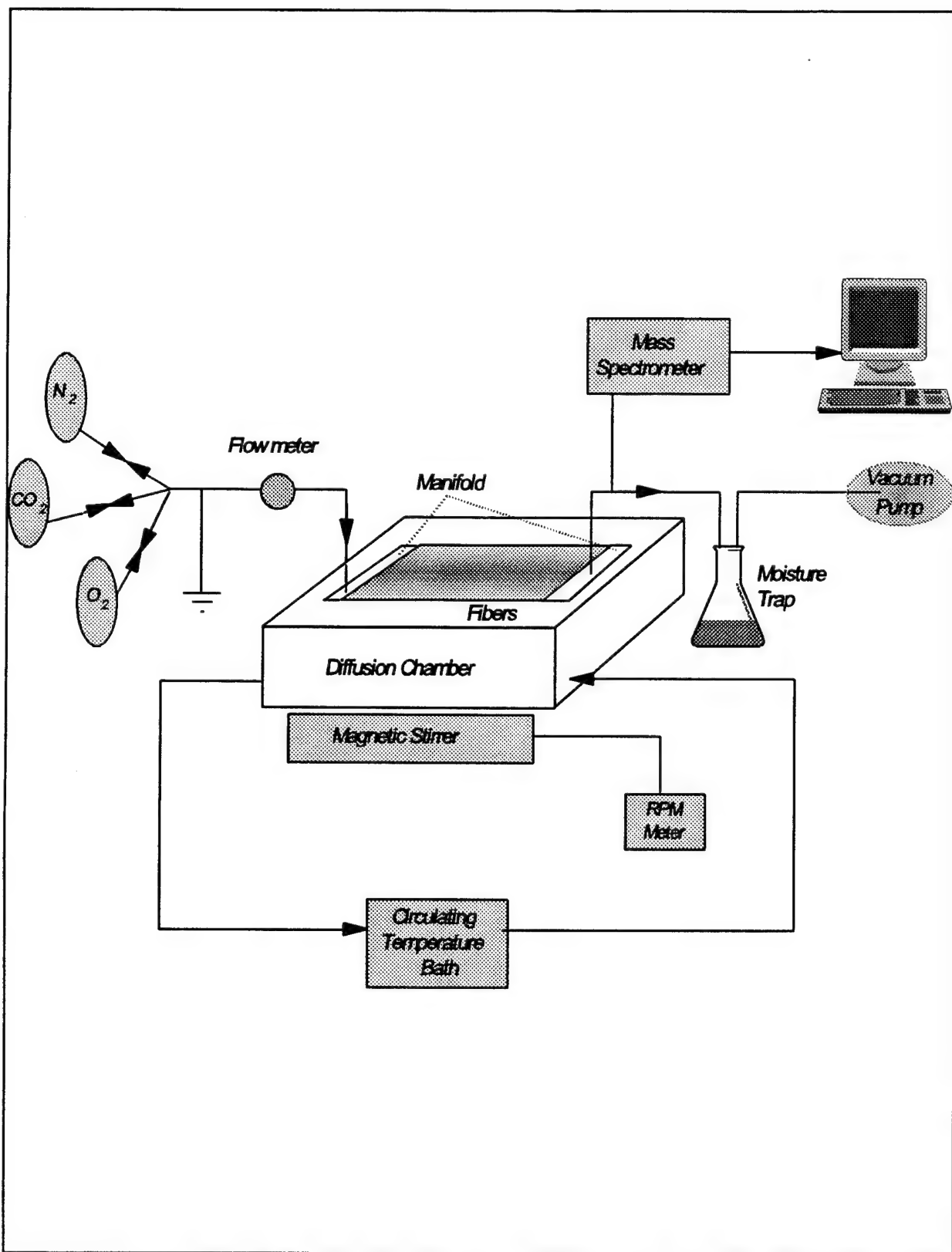


Figure 3.1 Schematic of diffusion chamber apparatus for measuring fiber permeability.

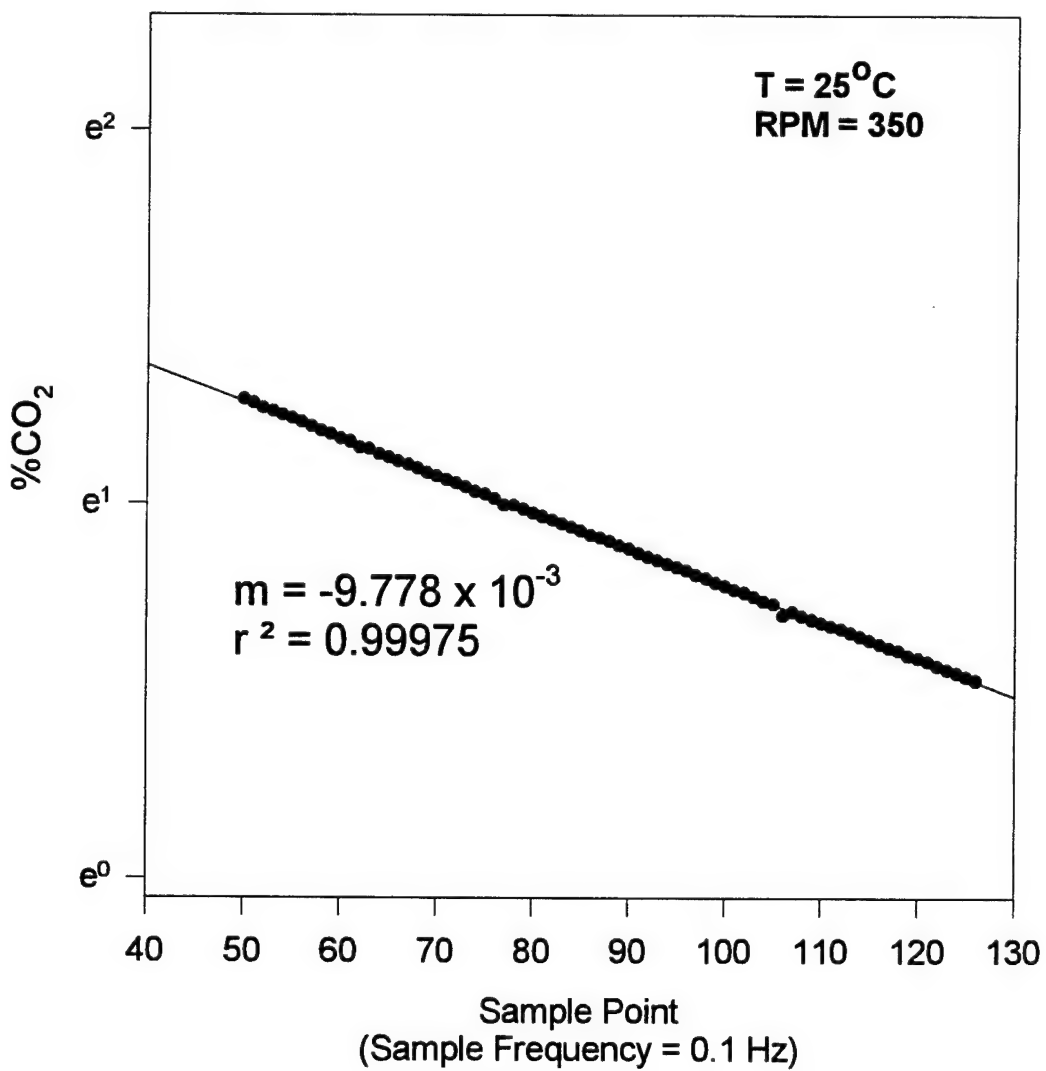


Figure 3.2  $\text{CO}_2$  concentration exiting fiber during washout.

### 3.3 Data Analysis

Calculation of the effective system permeability and subsequent fiber permeability from the species concentration measurements at the outlet of the fibers is based on simple mass balances, as outlined below.

*Calculation of Effective Mass Transfer Coefficient.* Performing a species mass balance in the liquid phase results in the following relation for the partial pressure of the species:

$$\frac{dP_o}{dt} = -\frac{KA}{\alpha V} [P_o(t) - \bar{P}_f(t)] \quad (3.1)$$

where  $\bar{P}_f(t)$  is the average pressure in the fiber at time t,  $P_o(t)$  = partial pressure of mass species ( $O_2$  or  $CO_2$ ) in the liquid at time t (mmHg), K = mass transfer coefficient of fiber/liquid system (ml gas at S.T.P./cm<sup>2</sup>/s/cmHg), A = total fiber surface area (cm<sup>2</sup>), V = volume of liquid in chamber (ml), and  $\alpha$  = solubility of the mass species in liquid (ml gas at S.T.P./ml/cmHg). Likewise, a mass balance for the same species in the gas phase yields,

$$\frac{d}{dz} [Q\gamma P_f(z,t)] = K \frac{dA}{dz} [P_o(t) - P_f(z,t)] \quad (3.2)$$

where,  $\gamma = 1/P_{atm}$  and Q = gas flow rate through the fibers (ml/s). These equations define a time constant,  $\tau$ , given by,

$$\frac{1}{\tau} = \frac{KA}{\alpha V}, \quad (3.3)$$

which corresponds to the time scale required to remove the  $O_2$  or  $CO_2$  from the chamber volume. We are interested in isolating the effect of the properties of the fiber membrane on mass transfer. The relation for the time constant (Eq. 3.3) assumes that the gas flow rates are sufficiently high such that gas flux is not flow dependent. This requires that  $Q\gamma \gg KA$ , a condition which is met by our procedure. Conversely, the gas flow should not be so high as to result in outlet  $O_2$  or  $CO_2$  concentrations which are too low for accurate measurement by the gas analyzer. The optimal flow

rate can be found experimentally, by comparing values of  $1/\tau$  measured at different gas flow rates to verify that it remains constant.

The partial pressure of  $O_2$  or  $CO_2$  measured at the outlet of the fibers decays with time constant  $\tau$ , and is thus given by,

$$P(L,t) = P_i'(L) e^{-\frac{KA_f}{\alpha V_t}} \quad (3.4)$$

Accordingly, the mass transfer coefficient,  $K$ , can be determined by fitting a line to a plot of the natural log of  $P(L,t)$  versus time, where the slope of the line is  $-KA/\alpha V$ .

Calculation of Membrane Permeability. The mass transfer coefficient,  $K$ , reflects overall resistance to mass transfer, and includes contributions from the liquid boundary layer as well as the fiber wall. The overall resistance to mass transfer,  $1/K$ , is determined from the resistances of the membrane and fluid in series as was shown in Equation 2.2 of section 2.1. The permeability of the boundary layer,  $K_l$ , is proportional to the liquid stir rate and is assumed to follow  $K_l = a\Omega^\beta$ , where  $\Omega$  is the liquid stir rate (rpm). Thus,

$$\frac{1}{K} = \frac{1}{K_m} + \frac{1}{a\Omega^\beta} \quad (3.5)$$

The exponent,  $\beta$  is -2/3 for stirred liquids (Brodkey, 1988). Determining  $K_m$  therefore involves fitting a line to  $1/K$  vs.  $(1/\Omega)^{2/3}$  and determining the intercept,  $1/K_m$  (Wilson analysis). Alternatively, non-linear regression can be used to fit a curve of the above form (Eq. 3.5) to  $K$  vs.  $\Omega$ , to determine  $K_m$ , as well as  $a$  and  $\beta$ . We are in the process of evaluating which procedure is most appropriate.

### 3.4 Permeability of MHF 200L Composite Fibers

Preliminary permeability measurements have been made for the Mitsubishi multi-layer hollow fiber (MHF) 200L composite membranes. The MHF 200L membranes consist of a one

micron thick polyetherurethane (PEU) true membrane layer supported between two microporous layers. Figure 3.3 shows a summary of the permeability measurements made for O<sub>2</sub> and CO<sub>2</sub> over a range of stir rates. As stir rate increases, the boundary layer resistance decreases and the permeability improves. Using these values, the fiber permeability is calculated using a Wilson plot as shown in Figure 3.4. The permeability of this fiber in water at 25°C was measured to be  $6.8 \times 10^{-6}$  ml gas (S.T.P.)/cm<sup>2</sup>/s/cmHg for oxygen, and  $5.6 \times 10^{-6}$  ml gas (S.T.P.)/cm<sup>2</sup>/s/cmHg for carbon dioxide.

Prior to performing these measurements it was assumed that the permeability of the MHF 200L fibers was less than that of the microporous fibers, but great enough to have a negligible effect on overall oxygen transport resistance. However, to meet the design criteria for an O<sub>2</sub> exchange rate of 135 ml/min, the effective permeability of our intravenous oxygenator must be on the order of  $1 \times 10^{-5}$  ml/cm<sup>2</sup>/s/cmHg, as depicted in Figure 2.1. The effective permeability of the IMO device will always be less than the smallest of the liquid phase and fiber permeabilities. Thus our measurements suggest that the maximum effective permeability of an IMO device constructed with MHF 200L fibers would only be  $6.8 \times 10^{-6}$  ml/cm<sup>2</sup>/s/cmHg in the limit of negligible liquid side mass transport resistance. This estimate is below that required to achieve the desired 135 ml O<sub>2</sub>/min exchange goal. Accordingly, if these measurements are supported by further work, the MHF 200L fiber may not be suitable for intravenous oxygenation devices like ours. We are continuing to perform permeability measurements of the MHF 200L fibers at 37°C to provide a measure of comparison for testing of other fibers, and for the purpose of determining  $\beta$ , as detailed previously.

### **3.5 Future Work in Fiber Evaluation**

In addition to the Mitsubishi MHF 200L fibers, we are also conducting permeability tests of the Mitsubishi KPF microporous hollow fiber membranes. Following measurements of their short term permeability, long term tests will be performed in water to study the effects of wetting. As described in Section 2.2, microporous fiber permeability is markedly affected by the degree of fluid infiltration of the pores. Long term measurements of fiber permeability in water and

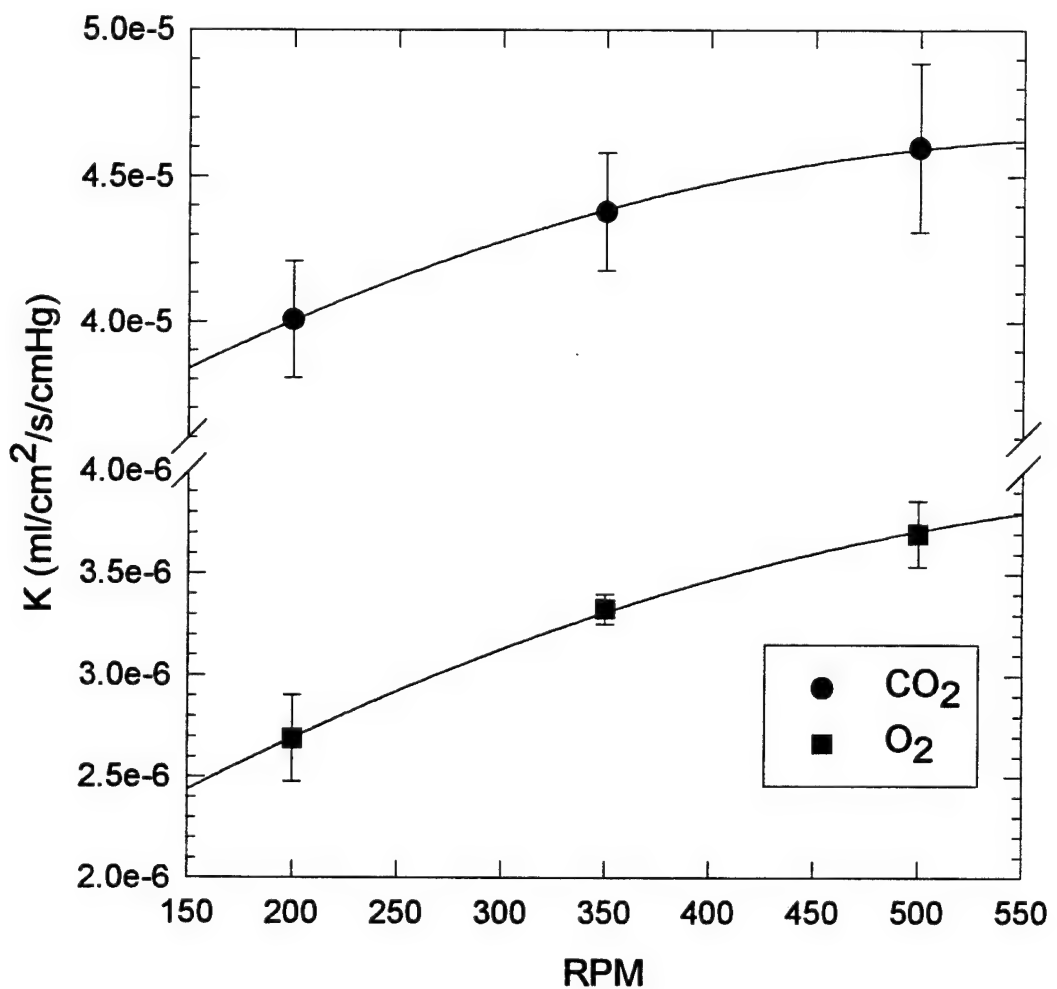
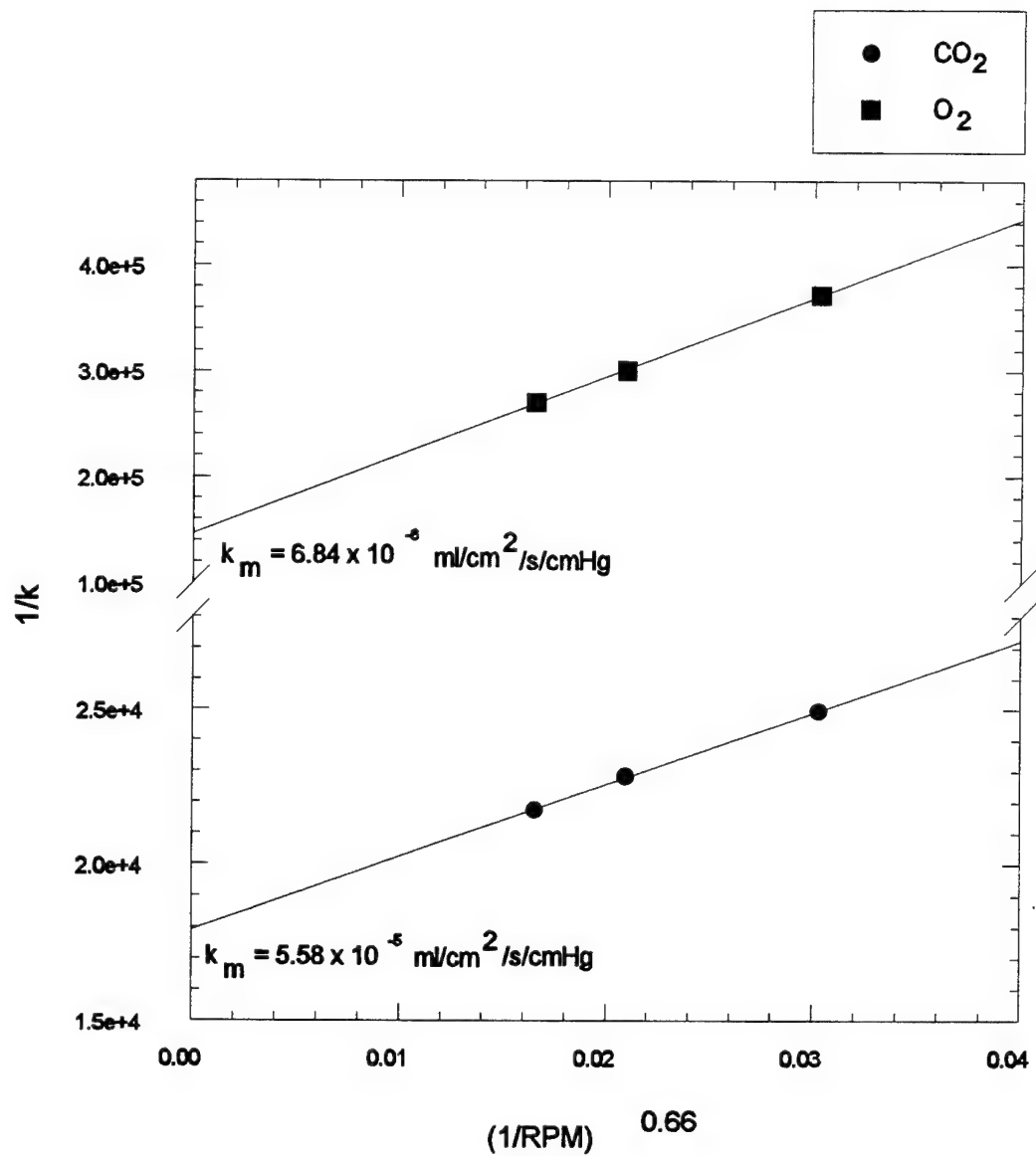


Figure 3.3 Overall permeability,  $K$ , for  $\text{O}_2$  and  $\text{CO}_2$  at different stir rates.



**Figure 3.4** Wilson plot of  $\text{O}_2$  and  $\text{CO}_2$  permeability measurements at varied stir rates. The intercept is  $1/K_m$ , the fiber permeability.

ultimately in plasma and blood will provide a means of identifying the causes of fluid infiltration and subsequent fiber permeability degradation.

We are also testing other composite fiber membranes. Samples have been received of a different composite fiber (Kuraray, Japan) which has a true membrane outer layer covering a microporous wall. In addition to promising the potential of higher permeabilities, this fiber may also enhance long term performance because the fiber pores are not exposed to liquid and are thus protected from wetting. An alternative Mitsubishi composite fiber (MHF u series) is also being acquired which has a thinner (1/2 micron) true membrane layer between the microporous outer layers. Additionally, a collaborative agreement is being established with Bend Research, Inc., for the development of a hollow fiber membrane designed specifically for intravenous membrane oxygenation. Bend Research has the capability to custom coat microporous fibers with thin silicone layers. The thickness of these layers can be specified based on the permeability desired of the fiber. As with the microporous fibers, testing of all composite fibers will involve short and long term permeability measurements.

Finally, we also plan to test the effects of the antithrombic, Carmeda coating on the permeability of promising fiber candidates.

## **4. IMO PROTOTYPE DEVELOPMENT**

The University of Pittsburgh Intravenous Membrane Oxygenator (IMO) is currently in a focused development phase of the Prototype D devices described in the Introduction. This section of the report summarizes the development work done on complete IMO prototype Ds over the past year. All prototypes are subjected to a standardized characterization test, which has been developed specifically to expedite the development phase of this project. An overview of the prototype development characterization test is given in 4.1, and performance results of prototypes tested thus far is presented in 4.2. A principal result of these characterization tests was identifying deficiencies in balloon pulsation (filling/emptying) associated with the pneumatics of the helium pathway within the IMO. As a result, the helium pathway is now being redesigned to alleviate these deficiencies, and we have developed special methodology to study the effectiveness of balloon pulsation, as described in 4.3. Related studies were also done on the gas flow dynamics within the O<sub>2</sub>/CO<sub>2</sub> pathway through the IMO device, and these studies are described in 4.4. Finally, this section ends with a brief summary of future development work for IMO prototypes.

### **4.1 Overview of Characterization Testing**

Rationale for Characterization Testing. We have designed and utilized a standardized prototype development characterization test (PDCT) which is specific to this phase of the project. The PDCT involves evaluating the exchange performance of prototypes in water, and allows for valid and expedient comparisons to be made among IMO prototypes as design changes are incorporated. Furthermore, the simplified PDCT has shortened the time associated with the iterative loop between design evaluation, design change/adjustment, and design re-evaluation. Accordingly, developmental progress toward our design goals can be realized more rapidly than if all prototypes were subjected to complete blood and *in-vivo* testing at this juncture in the developmental process. In addition, the process is more economical in that prototypes which undergo water testing are available for further design modification and re-evaluation. As a part of the PDCT, an engineering dimensionless analysis is used to *estimate* exchange performance in blood under physiological flow conditions from the *in-vitro* water characterization tests. This procedure allows assessing prototype performance vis-a-vis our ultimate design goal for exchange

in blood.

We plan to do the simplified PDCT in conjunction with design development until an IMO device is available which performs within 75 % of our design goal for exchange in blood (based on the estimating analysis described above). These candidate IMO devices will then undergo further, more elaborate characterization testing involving 1) *in-vitro* testing with blood, looking at gas exchange, flow resistance, and hemolysis generation; and 2) *ex-vivo* and *in-vivo* implants in adult male sheep.

Apparatus and Procedure. The gas exchange performance of IMO prototypes is characterized using an *in-vitro* mock loop, as depicted in Figure 4.1. The loop consists of a test section (*in-vitro* vena cava) in which the IMO device is placed, a Biomedicus pump and flowmeter (rotameter) to control fluid flowrate, a fluid reservoir, a temperature regulating heat exchanger, a deoxygenator, and various ports for taking samples and measuring pressure. Recently an expandable chamber was added to offer compliance to the system. An IMO device within the mock loop has separate gas pathways for oxygen delivery and removal, and for helium supply to the IMO balloon. The O<sub>2</sub> gas pathway includes an oxygen source, a Sierra gas flow meter, inlet and outlet pressure ports connected to a manometer, and a vacuum pump.

The protocol for mock-loop testing insures that all prototypes undergo characterization under equivalent steady state conditions. The prototype is placed in the loop, and O<sub>2</sub> gas is pumped through the fibers under vacuum at approximately -250 mmHg. The reservoir is then filled with 20L of deionized water, which is pumped through the loop at flowrates from 1 to 5 L/min. The heat exchanger is engaged and the system is allowed to equilibrate to 37°C. Nitrogen and oxygen gas are passed through the deoxygenator and oxygenator, respectively. An ABL 330 blood gas analyzer is used to measure the gas tensions of samples and is calibrated while the mock loop is reaching a steady state. The sampling protocol calls for measurements of the following parameters during a characterization run: gas partial pressures in the inlet and outlet water streams, atmospheric pressure taken from the ABL 330, gas flow rate, water flow rate, temperature of the loop, water inlet and outlet pressures, and balloon pulsation rate.

The samples for O<sub>2</sub> tension are drawn through two ports (inlet and outlet to the IMO-containing test section) that have a three-way stopcock connection. Connected to the two available

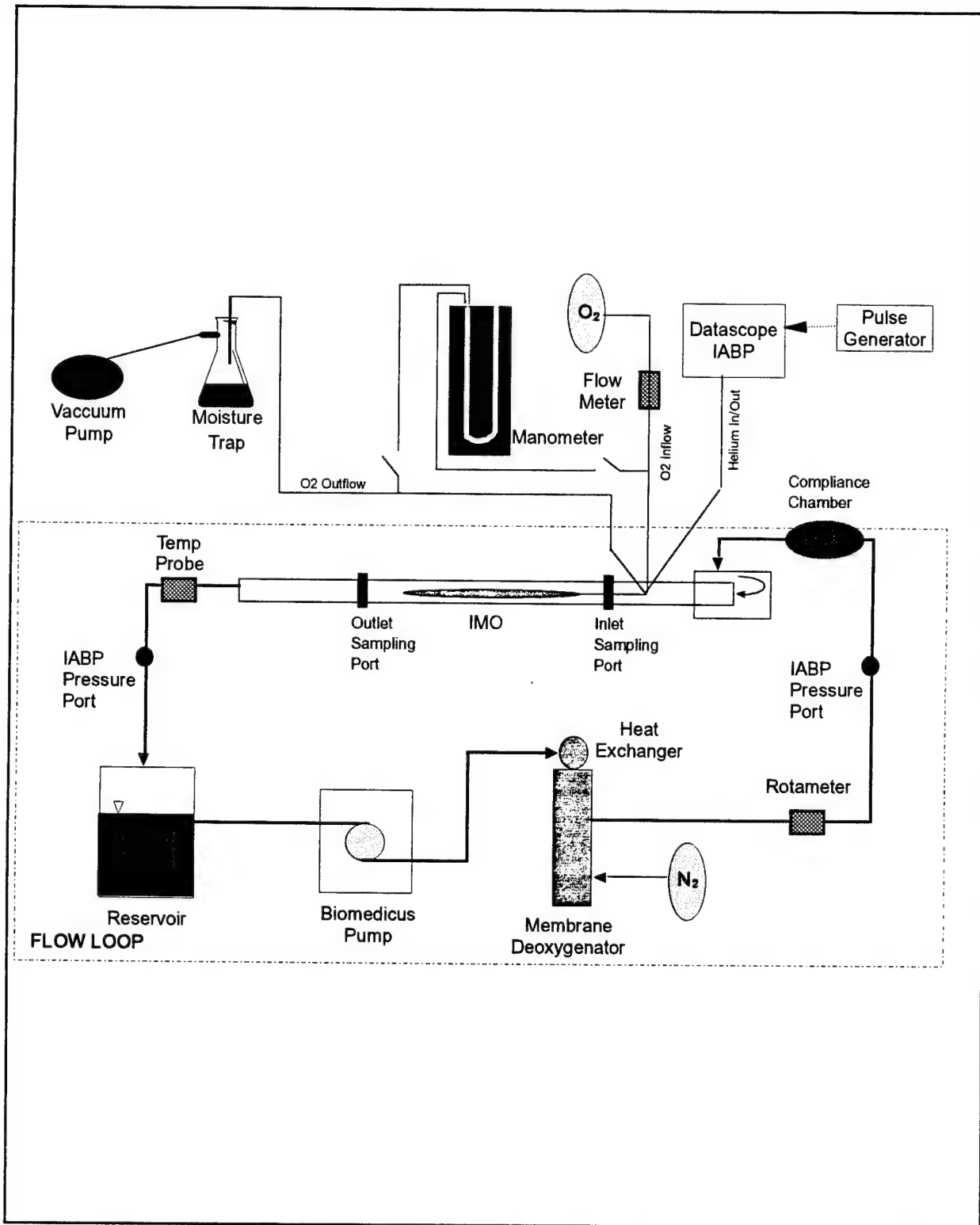


Figure 4.1 Diagram of mock loop used for *in-vitro* prototype characterization testing.

ports of the stopcock are a 10cc syringe for flushing and a 1cc syringe for collecting the sample. The stopcock is flushed several times with the 10cc syringe, with the last stroke pulling water into the syringe. The stopcock is then closed to the larger syringe and the 1cc is flushed in the same manner. The amount of times necessary to flush is determined by the amount of gas bubbles visibly present after each stroke. Once it is determined that there are no extraneous gases in the sample syringe, it is immediately injected into the ABL for analysis. While the sample is being analyzed, the fluid pulled into the 10cc syringe is returned to the system. This is repeated until all samples for the set are collected and recorded. The parameters are then changed to the next desired set and the system is allowed to reach steady state. After all data is obtained, the loop is drained and gas is vacuumed through the fibers to allow any moisture that has entered the gas pathway to dry. The data is entered into a computer spreadsheet for analysis, as described below.

*Documentation of Exchange Performance* The raw data from the characterization testing is entered into a standardized "Prototype Characterization Data Summary" spreadsheet, an example of which is shown in Figure 4.2. Within the spreadsheet, calculations of mean inlet and outlet PO<sub>2</sub> and PO<sub>2</sub> differences are performed. The data sheet information is used to calculate the mean intra-fiber pressure, mass transfer rate, mass transfer rate per unit surface area, device mass transfer coefficient, and actual water flow rate, using the following equations. Mean intra-fiber pressure, (P<sub>i</sub>), which is assumed to be equivalent to the mean intra-fiber PO<sub>2</sub> (because of the small volume fraction of CO<sub>2</sub>) is calculated from the equation,

$$P_i = \frac{(P_{atm} - P_{inlet\_gas}) + (P_{atm} - P_{outlet\_gas})}{2} \quad (4.1)$$

Mass transfer rate (VO<sub>2</sub>) is found using,

$$VO_2 = \alpha Q (PO_{2_{outlet\_water}} - PO_{2_{inlet\_water}}) \quad (4.2)$$

where  $\alpha$  is O<sub>2</sub> solubility in water at 37°C and Q is the water flow rate.

Prototype Characterization Test Summary

Prototype Specifications:											
Prototype Serial #:			D04			D04			D04		
Fiber Type:			GFF-18044			D02			D02		
Number of Fibers:			1000			D02			D02		
Length of Fibre (cm)			20			D02			D02		
OD of Fibre (mm):			0.0045			D02			D02		
ID of Fibre (mm):			0.02			D02			D02		
Tot. Fiber Surf. Area (mm²):			1551.75			D02			D02		
Material Properties:											
Material:			D04			D04			D04		
Base:			Glass			Glass			Glass		
Poisson's Ratio:			0.23			0.23			0.23		
Elastic Modulus (GPa):			70			70			70		
Shear Modulus (GPa):			27.3			27.3			27.3		
Young's Modulus (GPa):			105			105			105		
Tensile Strength (MPa):			345			345			345		
Compressive Strength (MPa):			450			450			450		
Flexural Strength (MPa):			100			100			100		
Tensile Modulus (GPa):			10.5			10.5			10.5		
Shear Modulus (GPa):			3.85			3.85			3.85		
Young's Modulus (GPa):			20			20			20		
Tensile Strength (MPa):			100			100			100		
Compressive Strength (MPa):			150			150			150		
Flexural Strength (MPa):			30			30			30		
Tensile Modulus (GPa):			1.5			1.5			1.5		
Shear Modulus (GPa):			0.5			0.5			0.5		
Young's Modulus (GPa):			1.5			1.5			1.5		
Mechanical Properties:											
Material:			D04			D04			D04		
Base:			Steel			Steel			Steel		
Flow Stress (MPa):			200			200			200		
Yield Stress (MPa):			180			180			180		
Tensile Strength (MPa):			400			400			400		
Elongation at Break (%):			10			10			10		
Modulus of Elasticity (GPa):			210			210			210		
Shear Modulus (GPa):			77			77			77		
Young's Modulus (GPa):			210			210			210		
Tensile Modulus (GPa):			21			21			21		
Shear Modulus (GPa):			77			77			77		
Young's Modulus (GPa):			210			210			210		
Tensile Modulus (GPa):			21			21			21		
Shear Modulus (GPa):			77			77			77		
Young's Modulus (GPa):			210			210			210		
Tensile Modulus (GPa):			21			21			21		
Shear Modulus (GPa):			77			77			77		
Young's Modulus (GPa):			210			210			210		
Tensile Modulus (GPa):			21			21			21		
Shear Modulus (GPa):			77			77			77		
Young's Modulus (GPa):			210			210			210		
Tensile Modulus (GPa):			21			21			21		
Shear Modulus (GPa):			77			77			77		
Young's Modulus (GPa):			210			210			210		
Tensile Modulus (GPa):			21			21			21		
Shear Modulus (GPa):			77			77			77		
Young's Modulus (GPa):			210			210			210		
Tensile Modulus (GPa):			21			21			21		
Shear Modulus (GPa):			77			77			77		
Young's Modulus (GPa):			210			210			210		
Tensile Modulus (GPa):			21			21			21		
Shear Modulus (GPa):			77			77			77		
Young's Modulus (GPa):			210			210			210		
Tensile Modulus (GPa):			21			21			21		
Shear Modulus (GPa):			77			77			77		
Young's Modulus (GPa):			210			210			210		
Tensile Modulus (GPa):			21			21			21		
Shear Modulus (GPa):			77			77			77		
Young's Modulus (GPa):			210			210			210		
Tensile Modulus (GPa):			21			21			21		
Shear Modulus (GPa):			77			77			77		
Young's Modulus (GPa):			210			210			210		
Tensile Modulus (GPa):			21			21			21		
Shear Modulus (GPa):			77			77			77		
Young's Modulus (GPa):			210			210			210		
Tensile Modulus (GPa):			21			21			21		
Shear Modulus (GPa):			77			77			77		
Young's Modulus (GPa):			210			210			210		
Tensile Modulus (GPa):			21			21			21		
Shear Modulus (GPa):			77			77			77		
Young's Modulus (GPa):			210			210			210		
Tensile Modulus (GPa):			21			21			21		
Shear Modulus (GPa):			77			77			77		
Young's Modulus (GPa):			210			210			210		
Tensile Modulus (GPa):			21			21			21		
Shear Modulus (GPa):			77			77			77		
Young's Modulus (GPa):			210			210					

**Figure 4.2** Documentation of prototype characterization testing and gas exchange performance.

The mass transfer coefficient, K, is determined from the equation,

$$K = \frac{\alpha Q}{A_f} \ln \frac{P_i - PO_{2_{inlet,water}}}{P_i - PO_{2_{outlet,water}}} \quad (4.3)$$

where  $A_f$  is the total surface area and  $\alpha$  and  $Q$  are the same as above. The actual water flow rate is calculated from an experimentally determined calibration curve specific to the flowmeter (rotameter) being used. Once all data for characterization of a particular prototype has been completed and analyzed, the various  $VO_2$ 's per surface area and the mass transfer coefficient, K, are plotted against water flow rate to compare to other prototypes.

*Prototype Logging.* Documentation has also been formalized to record IMO prototype device histories. A newly manufactured prototype receives a unique serial number, and all information specific to that prototype is entered into a prototype log book. Table 4.1 lists the parameters recorded into the log book for the five prototypes received over the past year. Four of the prototypes were standard Prototype D series devices. IMO Prototype D-01 and D-02 have tripartite balloon designs. Prototype D-01 was modified, however, to a unipartite design after insufficient balloon filling was apparent with the tripartite design. IMO Prototype D-03 was made specifically with the unipartite balloon design. IMO Prototype D-04 has a unipartite balloon and a modified helium pathway to improve balloon pulsation (see Section 4.3)

IMO Prototype OB-401 was a test design of a concept for keeping fibers within a bundle segregated, thus creating better contact between the fibers and the water flow field. Fibers are "tied" closely to the central gas delivery tube at three areas, resulting in four bulbous sections (hence the acronym OB for onion bulb). Prototype OB-401 does not incorporate a balloon within the fiber bundle.

**Table 4.1 Parameters of Prototypes Used in IMO Development**

Device Serial Number	Date Recv'd	Fiber Type	Fiber Number	Fiber OD(cm)	Fiber ID(cm)	Fiber Length (cm)	Total Fiber Surface Area(cm <sup>2</sup> )	Balloon Type
D-01	Feb15 1995	MHF- 200L	960	.02624	.02094	34	2690.7	Tripart. (40cc)
OB-401	Feb15 1995	MHF- 200L	1120	.02624	.02094	30	2769.8	None
D-02	Feb22 1995	MHF- 200L	960	.02624	.02094	34	2690.7	Tripart. (40cc)
D-03	Apr17 1995	MHF- 200L	960	.02624	.02094	34	2690.7	Unipart.
D-04	Jun6 1995	KPF- 190M	1008	.02450	.02000	20	1551.7	Unipart.

#### 4.2 Exchange Performance of Current Prototypes

*Results of Characterization Testing.* The performance of several of the IMO devices were evaluated using the prototype development characterization testing (PCDT). The performance of the prototypes evaluated are shown in Figures 4.3 and Figure 4.4. Results are shown as area normalized O<sub>2</sub> exchange rate versus water flowrate, Q.

Prototypes D01 (Figure 4.3) and D02 (Figure 4.4) were Prototype D IMO devices with tripartite balloons centrally incorporated within the fiber bundle. After several tests of D01 as a tripartite device (Figure 4.3, D01Tri), its balloon was modified into a single or unipartite balloon (Figure 4.3, D02Uni). For Prototype D01 in unipartite configuration, exchange performance was evaluated over the relevant flowrate range with balloon pulsation off (static), balloon pulsation off but balloon inflated (inflated), and balloon pulsations at 40, 60, and 120 bpm. In addition, it was also evaluated in a "scrunch" position (Figure 4.3, scrunch), in which the distance between inlet and outlet manifolds is shortened (by pulling back on the central feed tube), forcing

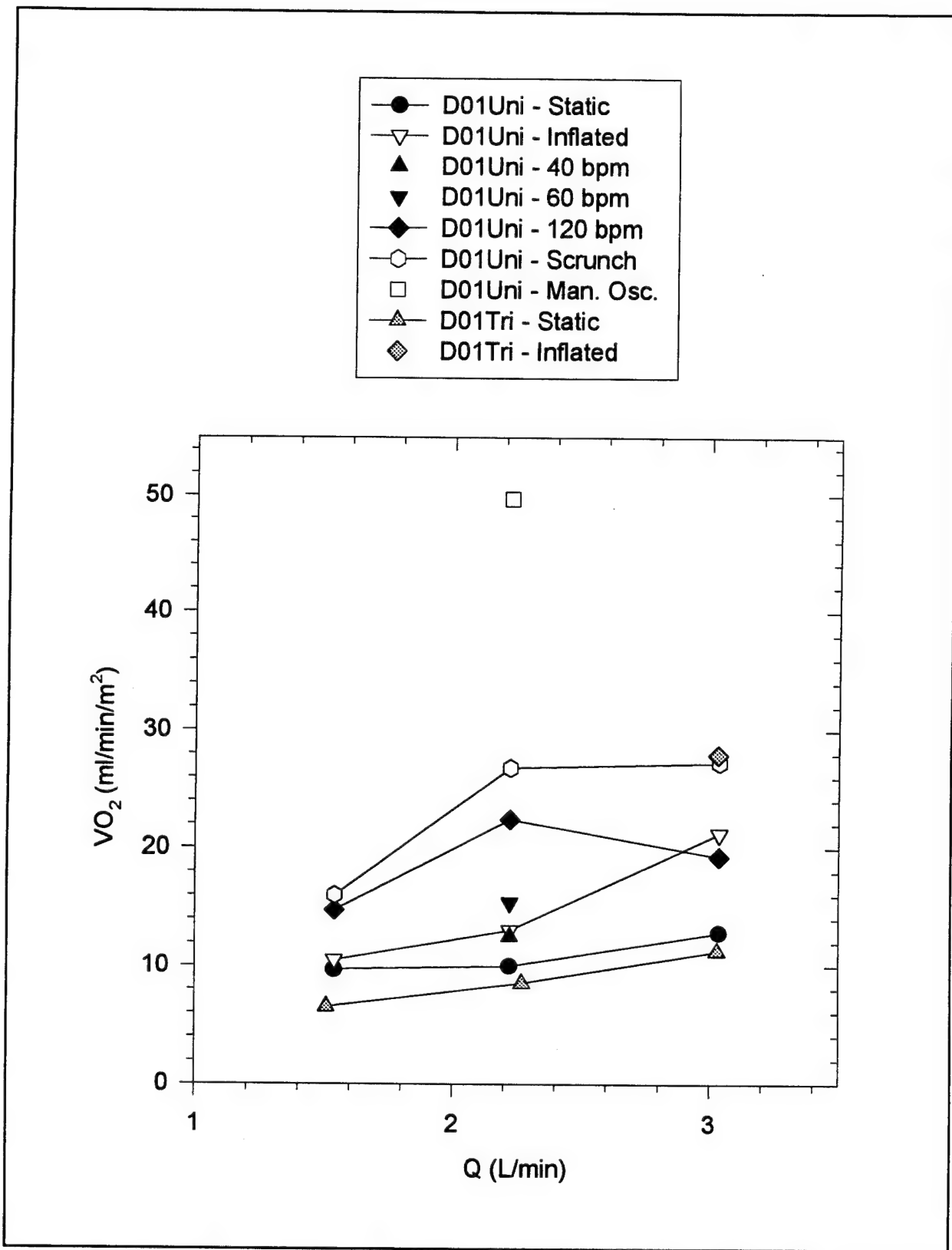


**Figure 4.3**  $\text{O}_2$  exchange performance of Prototype D01 from characterization testing

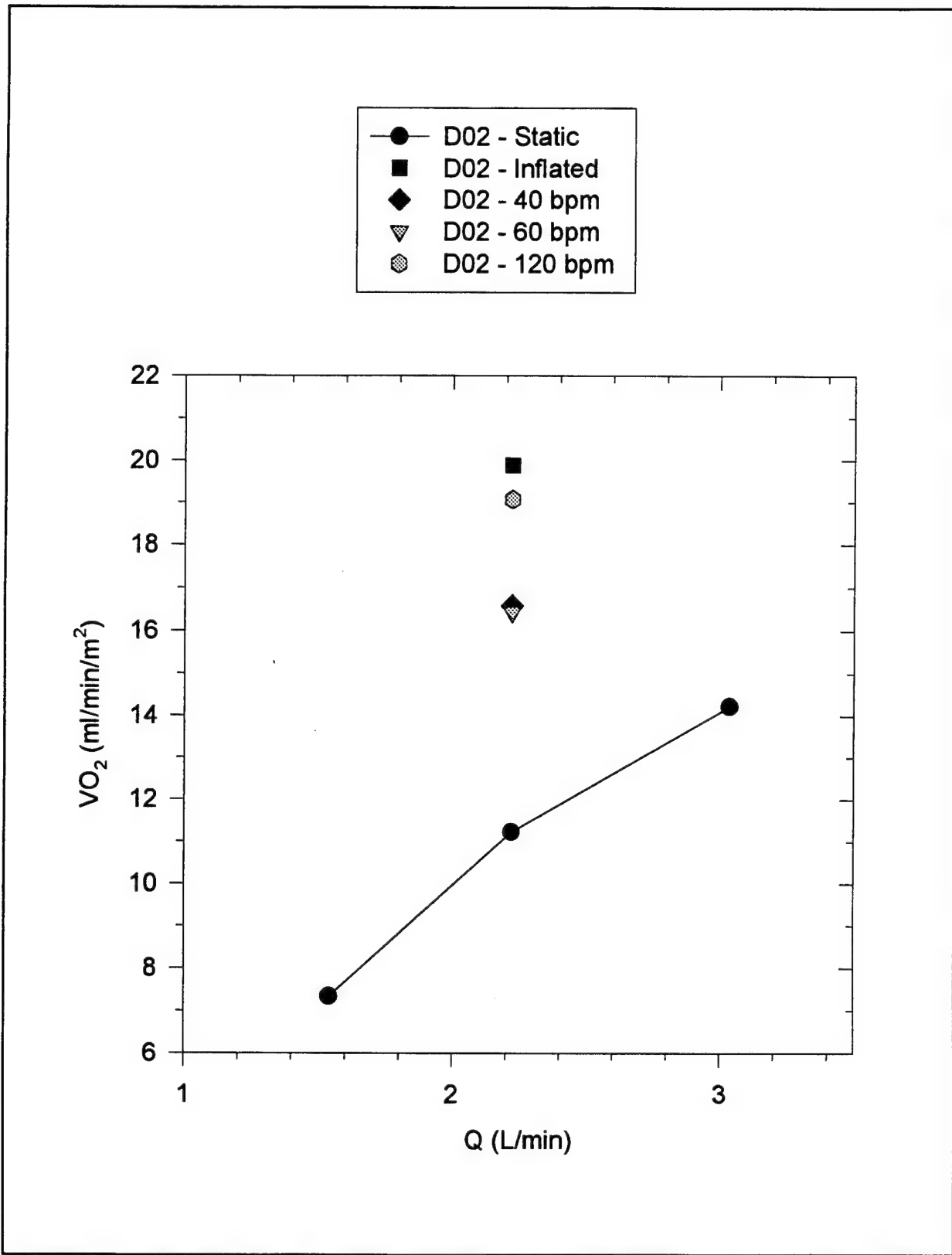


Figure 4.4  $O_2$  exchange performance of Prototype D02 form characterization testing.

the fibers outward to occupy a larger cross-section of the in-vitro vena cava. For Prototype D02, balloon pulsation was applied at only one flowrate ( $Q=2.1$  L/min).

Several important conclusions were made and actions taken based on the PCDT of D01 and D02. First, even with balloon pulsation, the general levels of levels of  $O_2$  exchange in water were relatively low (less than 30 ml/min/m<sup>2</sup>). In approximate terms, the exchange levels in blood would be larger by about an estimated factor<sup>2</sup> of four. Accordingly, the estimated exchange rate in blood would be less than 120 ml/min/m<sup>2</sup>, and hence exchange in a 0.5 m<sup>2</sup> device would be about 1/2 our exchange rate goal. *All evidence suggests that balloon pulsation was ineffective in these IMO prototypes.* For example, the normalized exchange rate for D01 at 120 bpm was less than with no balloon pulsation and the fibers in a scrunched position. Similarly, normalized exchange rate in D02 with the balloon static but inflated was higher than that with pulsation at 120 bpm. Thus, balloon pulsation was providing ineffective mixing in these IMO prototypes. *Accordingly, principal corrective action based on these characterization tests was to analyze the helium gas pneumatic system and the resulting effectiveness of balloon activation (filling/emptying).* The studies, conclusions and design changes associated with analyzing balloon pulsation effectiveness are described below in 4.3.

The PCDT of Prototypes D01 and D02 also suggested a potential alternative method for increasing mixing and augmenting exchange. A pilot test was done on Prototype D01 involving direct mechanical oscillation of the oxygenator fibers at 60 bpm (Figure 4.3. man. osc.). This was accomplished by oscillating the central gas feed tube of the device, which forces the fibers to oscillate outward and back in the cross-section of the in-vitro vena cava. The exchange rate associated with mechanical oscillation was 50 ml/min/m<sup>2</sup> for this pilot study, which was the largest exchange rate seen in the current PCDT. Accordingly, we are designing a mechanical activation system for Prototype D to further investigate gas exchange augmentation with direct mechanical activation of the fibers. The mechanical activation system converts rotary motion of

---

<sup>2</sup> An engineering analysis is used to estimate blood performance from water testing data. This analysis is described and discussed in the subsequent section. For quick estimates the factor of 4 described here appears consistent with this engineering analysis, as well as with past data of our group and of others looking at blood versus water exchange performance.

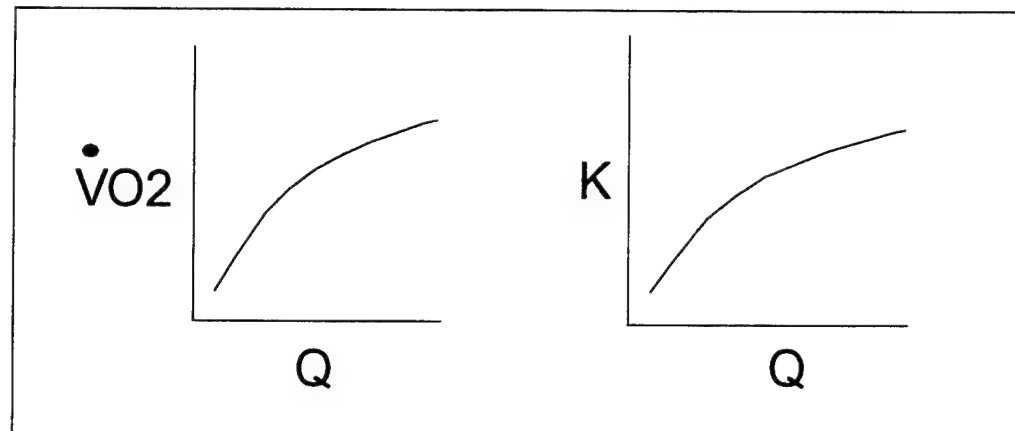
a drive motor to the rectilinear motion required to oscillate the central feed tube and fibers of the IMO device. An IMO prototype with the mechanical activation system should be available within the next month.

*Estimating Exchange Performance in Blood.* An engineering analysis can be used with PDCT to estimate exchange performance in blood from that in water. The analysis is based on that used and validated by Vaslef *et al.* (1994a and 1994b) for extracorporeal and intracorporeal artificial lungs. The overall procedure for estimating blood performance is summarized in Figure 4.5, and details can be found in Vaslef *et al.* (1994a). The PDCT in water yields the  $O_2$  exchange rate as a function of water flowrate,  $Q$ , through the *in-vitro* vena cava. Further reduction of this data provides the relationship between the effective exchange permeability (or mass transfer coefficient),  $K$ , of the IMO device and water flowrate. Using physical constants for water, the  $K$  versus  $Q$  relationship is expressed in suitable dimensionless form by introducing the Sherwood number ( $Sh$ ), the Schmidt number ( $Sc$ ), and the Reynolds number ( $Re$ ) (see Hines and Maddor, 1985). The ratio  $Sh/Sc^{1/3}$  essentially represents a normalized mass transfer coefficient, while the Reynolds number,  $Re$ , represents a normalized flowrate. Dimensional analysis indicates that the relationship between *normalized* mass transfer coefficient and flowrate should be independent of the fluid used with the IMO device, and hence should apply to blood. Accordingly, using appropriate physical constants for blood (see Vaslef *et al.*), the normalized relationship is converted back to a relationship between  $K$  and  $Q$  for blood flow with the IMO device. This relationship can then be cast in terms of  $O_2$  exchange rate versus blood flowrate.

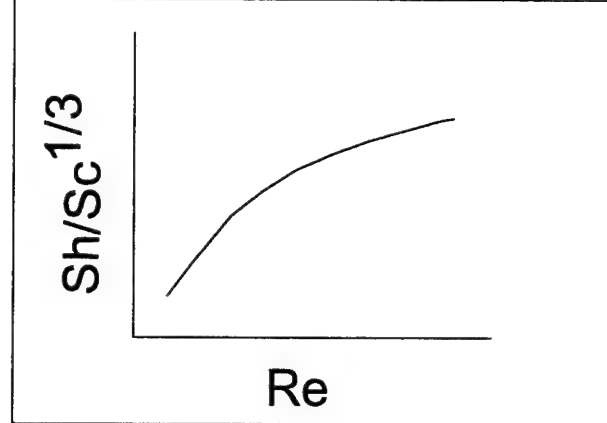
We have just started to incorporate this predictive scheme into data analysis from characterization testing, and Figure 4.6 shows some preliminary results. These results are based on recent characterization testing of Prototype D03 without balloon pulsation. The symbols show the actual experimental data for area normalized exchange rate versus flowrate through the *in-vitro* vena cava of the mock loop. The  $O_2$  exchange rate is relatively low because of the absence of active mixing via balloon pulsations. The solid lines, as indicated, are the predictions based on the engineering analysis for exchange in water and in blood with a venous  $O_2$  tension of 40 mmHg. These preliminary results indicate that the  $O_2$  exchange rate for the IMO device in blood is roughly 2.5 times that determined in water. Our experimental work with early prototypes

## Data Analysis and Reduction:

Water



Dimensional  
Analysis



Predictive Scheme:

Blood

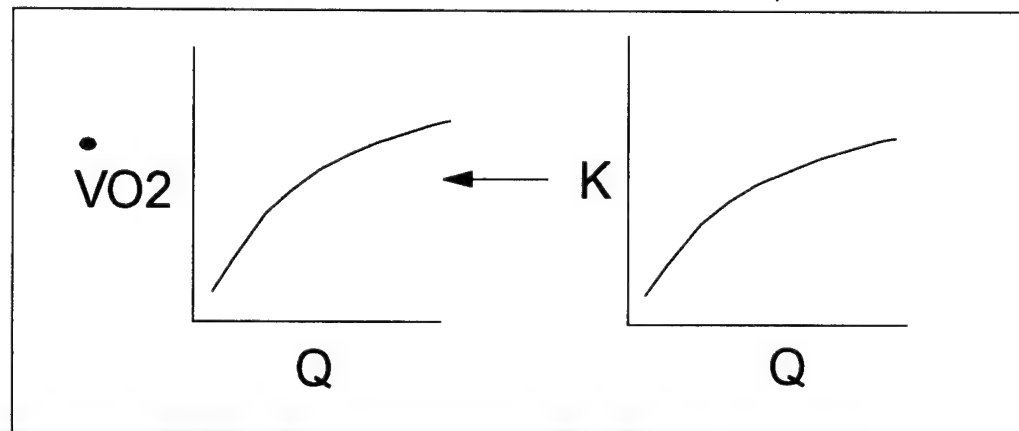


**Figure 4.5** Analysis procedure for estimating IMO gas exchange in blood from water characterization testing.

### Prototype D03 (6-7-95)

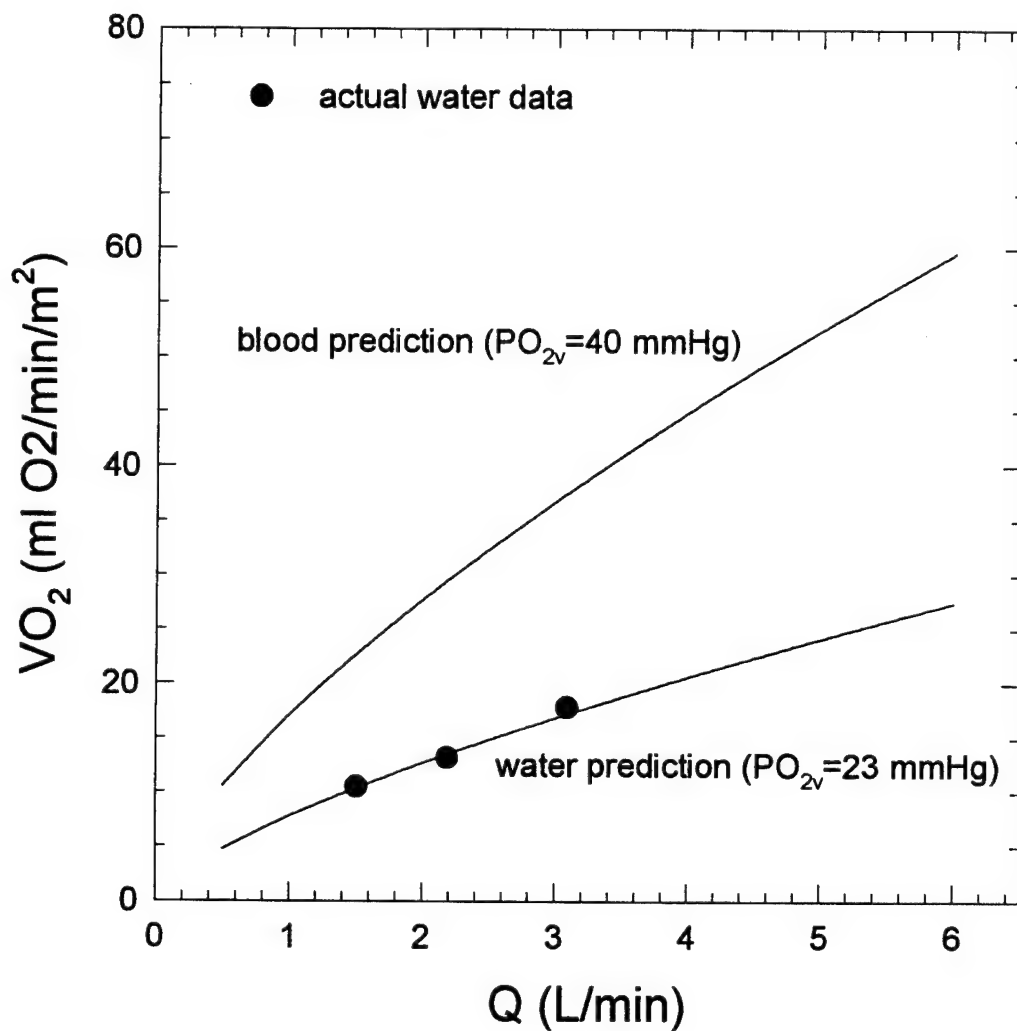


**Figure 4.6** Estimated exchange performance in blood from characterization testing in water for Prototype D03.

suggested a factor of between 3 and 4 for converting water exchange rates to those in blood. The results of Vaslef et al. (1994) in extracorporeal oxygenators suggest a factor of approximately 8 between blood and water exchange rates for O<sub>2</sub>. Thus, the predictive scheme may underestimate the O<sub>2</sub> exchange rate in blood, and hence provide a conservative estimate of exchange performance in blood. Accordingly, additional work will be done in the coming year to further validate this methodology and to better establish the factor relating O<sub>2</sub> exchange performance in blood to that in water.

#### 4.3 Analysis of Balloon Pulsation

Helium Pathway Pneumatics. The gas exchange performance obtained with our Prototypes D01 and D02 (see Section 4.2) indicated some potential problems with balloon pulsation within these prototypes. Accordingly, we conducted a design review of the helium delivery pathway of our IMO prototypes and the helium flow dynamics therein. The balloon pulsations are currently driven by a Datascope Intra-Aortic Balloon Pump (IABP) console. The complete helium pathway from the console to the balloon includes a 6 foot extender tube external to the IMO device, and internal to the IMO device are an introduction tube, a long annular pathway, and a short annular pathway. The critical dimensions of these pathways are listed in Table 4.2

Table 4.2 *Dimensions of Helium Pathway within IMO Prototype D*

pathway	outer diameter (in)	inner diameter (in)	length (in)
IMO introduction tube		0.076	2.5
long annular pathway	.148	.128	7.0
short annular pathway	.136	.128	1.4

We can use these dimensions to estimate the pressure drop required for balloon filling and emptying under relevant conditions. Helium flow during balloon filling and emptying is time-dependent. Nevertheless, the calibre of the pathways listed in Table 4.2 are sufficiently small that unsteady inertial effects are negligible, and the flow through the pathways can be considered

quasisteady. Accordingly, we can use standard relationships for the pressure drop and flowrate relationship for fully developed, steady laminar flow in tubes and in annular pathways. Filling and emptying a 40 ml balloon at 100 bpm represents an average helium flowrate during filling or emptying of  $Q=8$  L/min. This is so because the 40 ml volume must be delivered or removed in half the beat period:  $0.01 \text{ min}/2 = 0.005 \text{ min}$ , and hence  $Q=0.04 \text{ L}/0.005 \text{ min}=8 \text{ L/min}$ . At this flowrate the estimated pressure drop in the pathways listed above are: introduction tube, 4 mmHg; long annular pathway, 230 mmHg; and short annular pathway, 790 mmHg. The Datascope IABP helium drive system has a maximum drive pressure of 8 psi or about 410 mmHg. Thus, these estimates portend a serious pneumatic limitation to balloon pulsation in our current IMO device, driven by the Datascope IABP console.

To further support the pressure drop estimates, experimental measurements were made of the pressure drop and flowrate relationship for the helium pathway. These measurements were done by removing the balloon from Prototype D02 and applying an air vacuum to the helium delivery introduction tube of the IMO device. Thus, the pressure flow behavior corresponds to air flow through the helium pathway of the IMO device. Figure 4.7 shows the measured relationship between pressure and flow over a relevant range of conditions. The symbols correspond to the measured experimental data points. The helium pressure flow relationship is determined from the air relationship by multiplying the slope of the air data by the ratio of helium viscosity to that of air (helium gas is approximately 1.05 more viscous than that of air). Density differences need not be considered since the flow within the pathway is quasisteady. Also indicated in Figure 4.7 is the available drive pressure from the Datascope IABP system. These experimental results are consistent with the theoretical estimates given above, and indicate the potential for limitation in balloon pulsation as average helium flowrates approach the 8 L/min range.

The helium results in Figure 4.7 are recast in Figure 4.8 as required drive pressure versus balloon pulsation rate. The latter assumes filling and emptying a 40 ml helium balloon during the beat period associated with pulsation. Again, given the drive pressure associated with the Datascope IABP system, this analysis suggests a clear limitation to effective balloon pulsation with the current helium pathway. More specifically, balloon pulsation would become compromised at

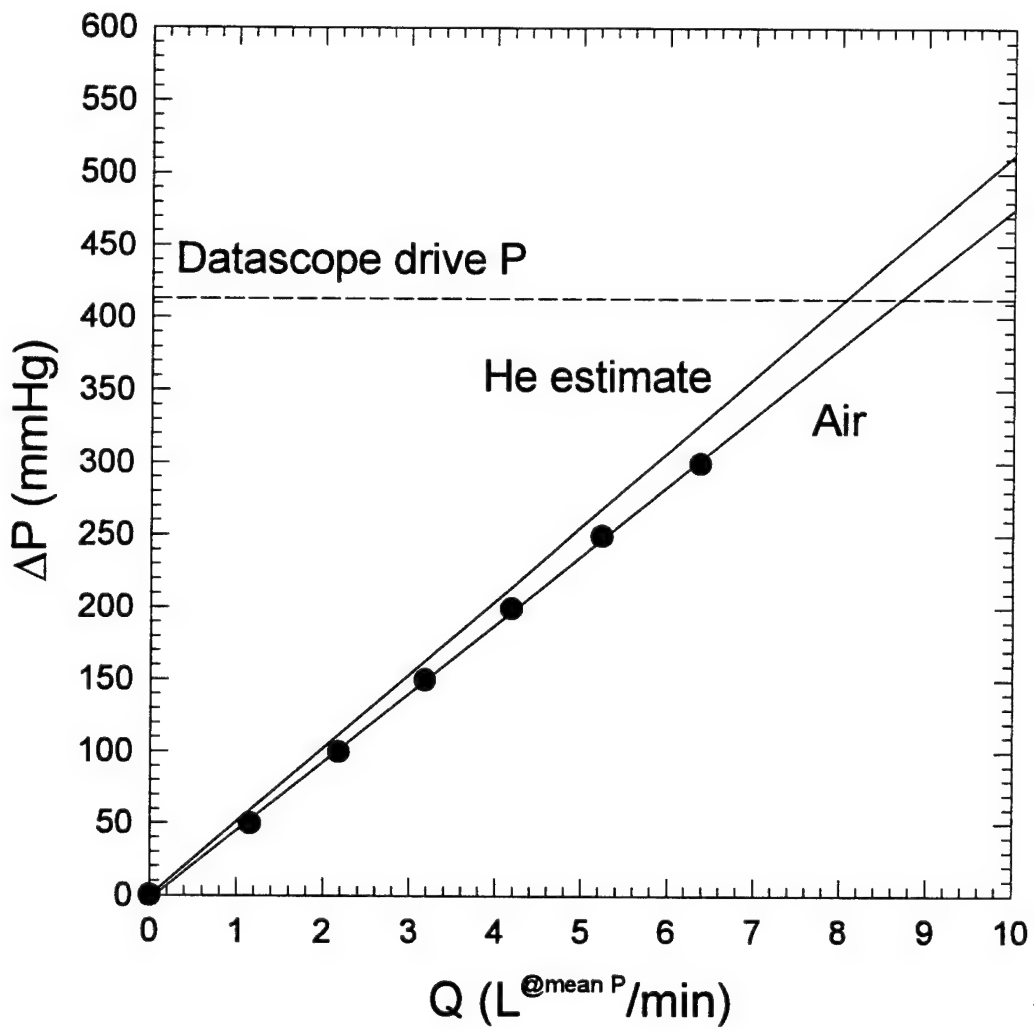


**Figure 4.7** Pressure and flowrate relationship for helium pathway in Prototype D02. Symbols represent experimental data for air; helium line determined from air regression line.

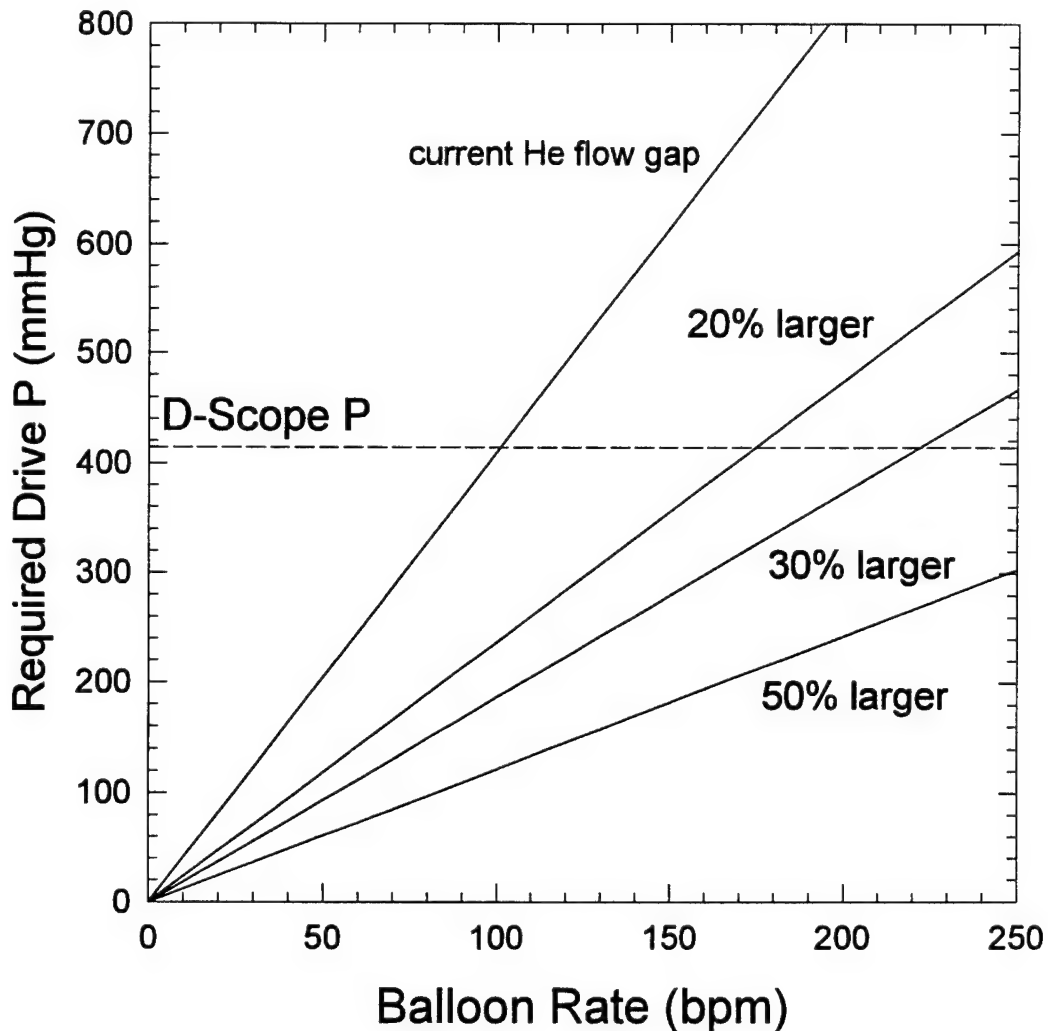


**Figure 4.8** Required drive pressure for pulsating 40 ml balloon in Prototype D with existing and with enlarged helium pathways.

rates approaching 100 bpm. Also, included in Figure 4.8 are the predicted relationships for balloon pulsation with 20%, 30% and 50% increases in the calibre (gap clearance) of the helium pathways within the IMO device. Increasing the helium flow gap by 30%, for example, may allow for effective balloon pulsations above 200 bpm. Thus, relatively small dimensional changes in the helium pathway may lead to substantially enhanced active mixing.

The analysis of the pneumatics associated with the helium pathway in our IMO device has resulted in an ongoing redesign of that pathway. In conjunction with redesigning the helium pathway, we have also built an apparatus for measuring the filling and emptying characteristics of balloons within intact IMO devices over a relevant range of frequencies. This provides us a tool to directly assess how design changes in the helium pathway impact on balloon filling and emptying. This apparatus and the associated studies are discussed in the next section.

*Frequency Spectrum of Balloon Pulsation.* We built a simple device to quantify balloon filling and emptying as a function of pulsation frequency in intact IMO devices. The apparatus is shown in Figure 4.9 and consists of a sealed chamber partially filled with water within which an IMO device is placed. Filling the IMO balloon compresses the air volume in the sealed chamber, and the resulting increase in system pressure is measured by a transducer placed within the water volume. The ratio of air to water within the chamber is adjusted so that the pressure oscillations associated with filling and emptying the IMO balloon are less than 20 mmHg, and hence only a small fraction of the drive pressure obtainable from the Datascope IABP system. A pressure volume curve for the system is determined to relate pressure changes to volume changes of the balloon. The characterization of balloon pulsations for an IMO device consists of driving the IMO balloon over a range of beat rates and recording the resulting box pressures, which are later converted to the inflation-deflation volume amplitude via the pressure volume calibration curves described above. These inflation-deflation volume amplitudes displayed as a function of frequency represent a frequency spectrum for balloon pulsation of a particular IMO device.

Figure 4.10 shows the frequency spectrum of balloon pulsation for IMO Prototype D03, which has an unmodified helium pathway (same pathway as in D01 and D02). Inflation and deflation of the balloon began to diminish at about 70 bpm, and by about 160 bpm complete cessation of balloon pulsation occurred. Figure 4.11 shows the same frequency spectrum for

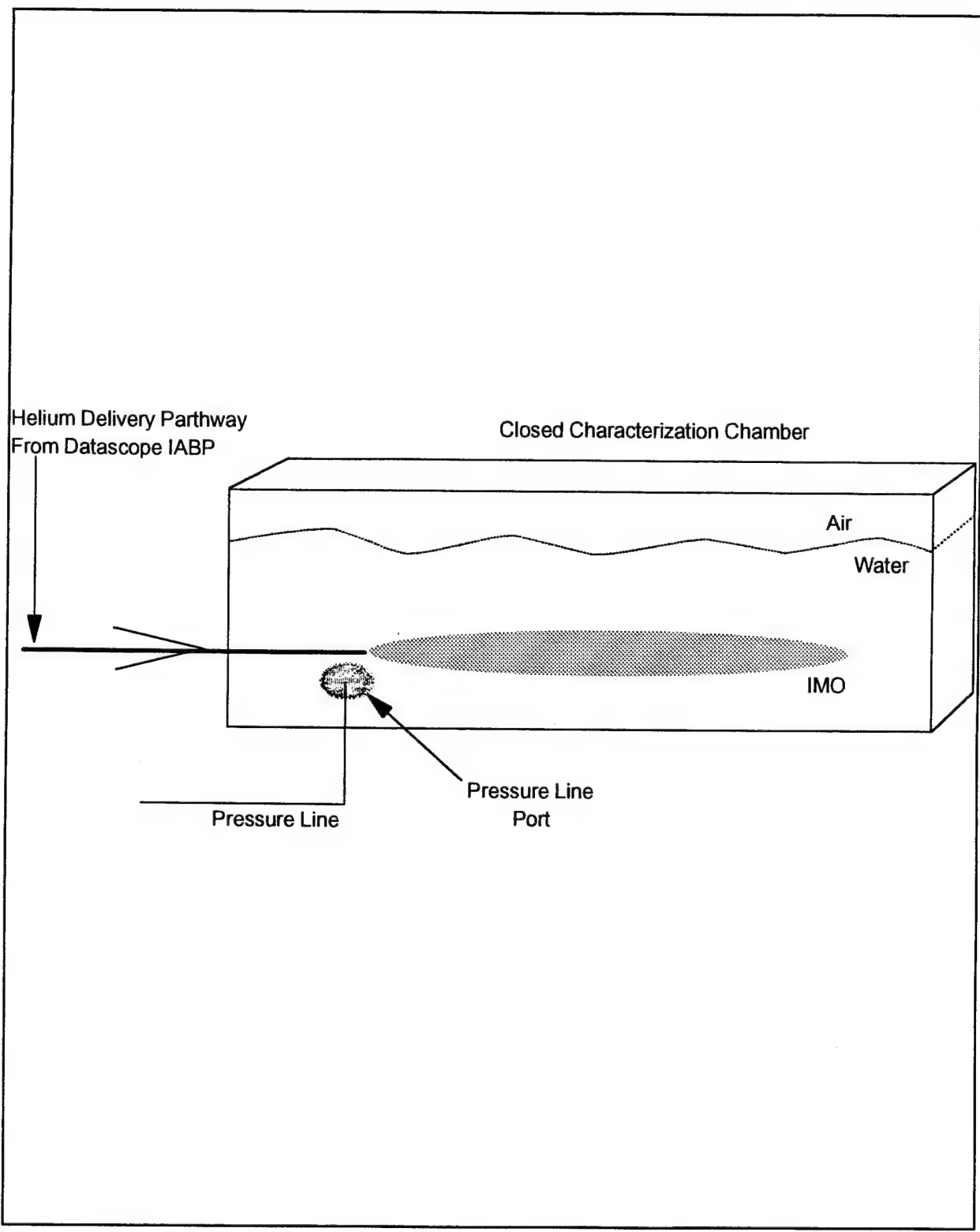


**Figure 4.9** Apparatus for determining frequency spectrum for balloon pulsation in IMO prototypes.

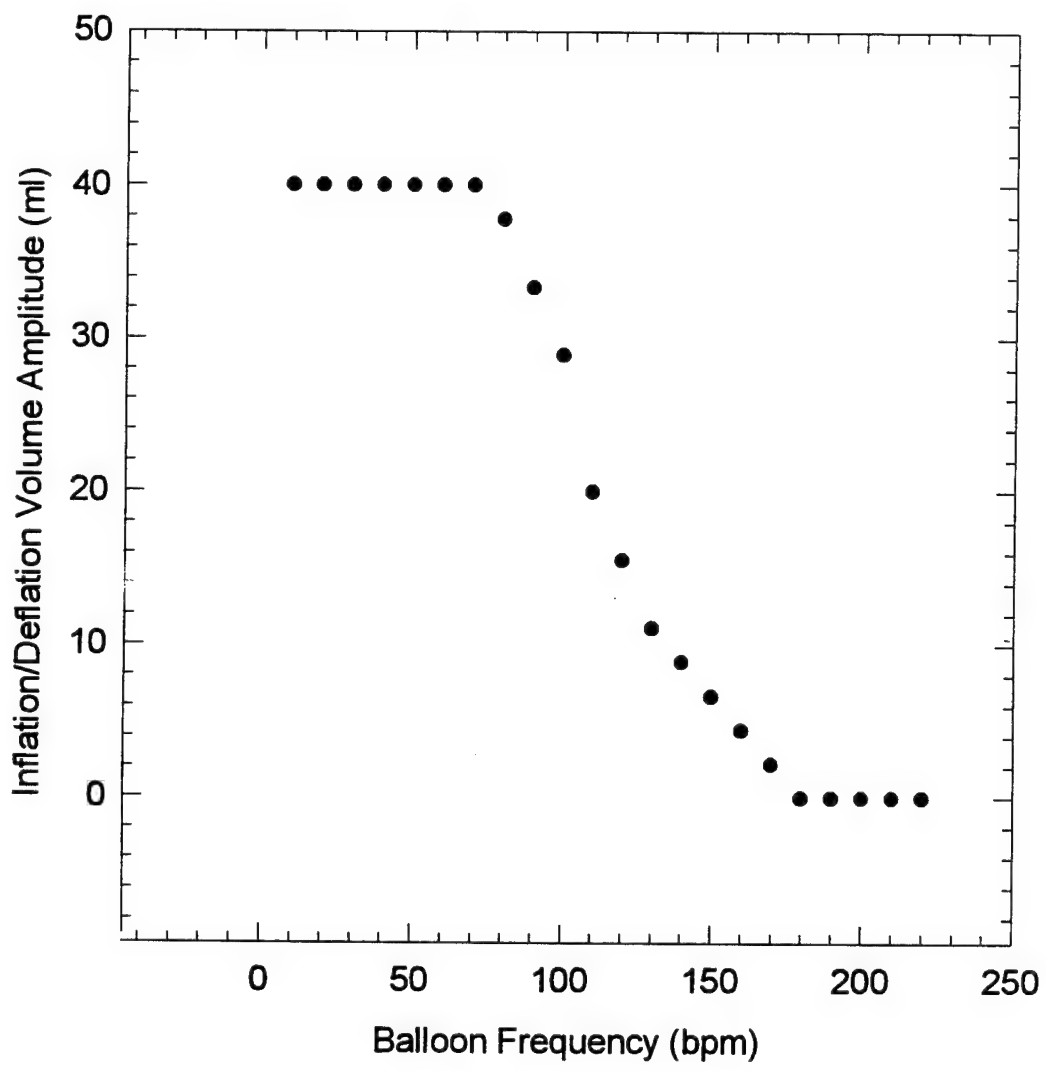


**Figure 4.10** Frequency spectrum of balloon pulsation for IMO prototype D03, with unmodified helium pathway.

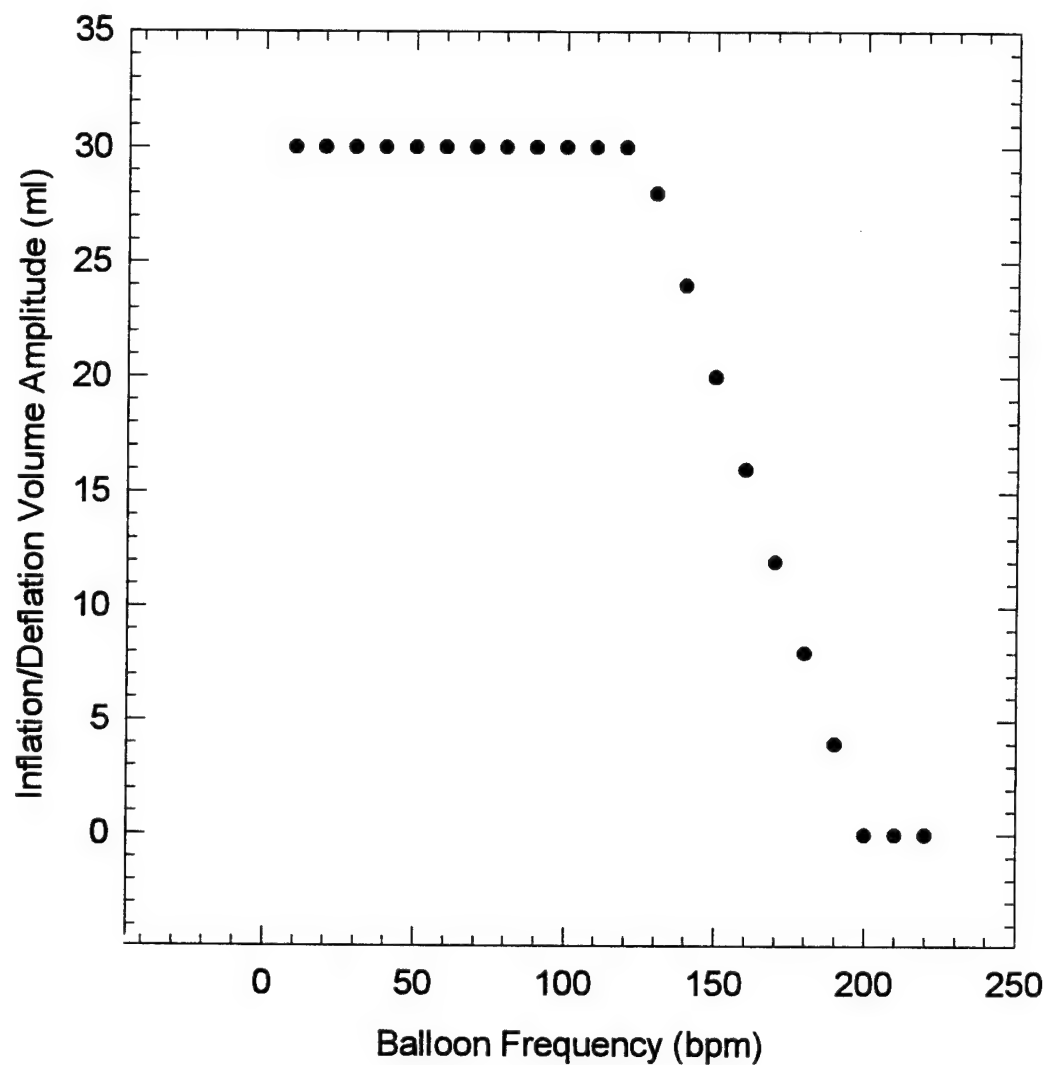


**Figure 4.11** Frequency spectrum of balloon pulsation in IMO Prototype D04, with modified helium pathway.

IMO Prototype D04. This prototype represents the first with modifications made to the helium pathway to improve helium gas flow. In addition, the prototype uses a 30 ml balloon rather than the 40 ml balloon used in Prototypes D01 through D04. Figure 4.11 indicates that full inflation and deflation is maintained up to about 120 bpm, and complete cessation of balloon pulsation does not occur until about 200 bpm. Thus, design changes to the helium pathway resulted in clear improvements in the balloon inflation and deflation dynamics. Prototypes D03 and D04 are currently undergoing gas performance characterization to establish the degree to which the improvements in balloon pulsation translate into improved gas exchange capability.

We expect that improvements in balloon pulsation will lead directly to better gas exchange performance of our IMO device. Accordingly, further review and design modification of the helium pathway within the IMO device is critical and will continue into the next contract year. The ability to measure the frequency spectrum of balloon pulsation for intact IMO devices provides a valuable tool for gauging progress along these lines.

#### 4.4 Gas Flow Dynamics in the IMO

*Rationale for Studies* The dynamics of intraluminal gas flow play a key role in exchange by setting the pressure variation along the length of the individual fibers. That is, as the gas species (fractional) concentration varies along the fiber due to the ongoing exchange processes, the species partial pressure within the fiber, a key element of exchange, depends directly on the variation of total gas pressure along the length of fiber. Accordingly, a quantitative description of the gas flow dynamics (pressure-flow behavior) within the fibers becomes a necessary prerequisite for a clearer understanding of the IMO exchange process itself.

The dynamics of gas flow within hollow fiber membranes may appear superficially as an application of simple incompressible Poiseuille flow theory. Owing to the small size of the fibers, however, coupled with their great length, flow resistance can be appreciable. Accordingly, the pressure drop can be relatively large, and variations in fluid density are potentially important. Thus, developing a clearer picture of the gas flow dynamics within an IMO device requires examining the influence of gas compressibility. An intravenous oxygenator by necessity possesses substantially fewer fibers per unit gas flow than clinically-used extracorporeal oxygenators.

Accordingly, in intravenous oxygenation devices, pressure variations are larger and gas compressibility effects are of greater potential importance for developing descriptive models of exchange.

*Relevant Background Theory.* Incompressible fully developed viscous flow in a tube follows Poiseuille's law, whereby the flowrate through the tube is linearly proportional to the pressure drop:

$$P_0 - P_L = RQ \quad (4.4)$$

where  $P_0$  and  $P_L$  are the fluid pressures at the inlet and outlet, respectively,  $Q$  is the volumetric flowrate of the fluid, and,  $R$  is the Poiseuille flow resistance of the tube. The Poiseuille flow resistance is given by  $R = 128 \mu L / \pi d^4$ , where  $\mu$  is fluid viscosity,  $L$  is the length of the tube and  $d$  is the tube diameter. The applicable theory for *compressible* Poiseuille flow is not easily found in compressible flow treatises, but a brief development is outlined in Williams et al (1995). The pressure flowrate relation for compressible Poiseuille flow is given by

$$P_0^2 - P_L^2 = 2RP_{atm}Q^{RTP} \quad (4.5)$$

where  $P_{atm}$  is atmospheric pressure, and  $Q^{RTP}$  is the mass flowrate in volumes of gas at reference temperature and pressure (RTP: 25°C and Patm). Thus, compressible Poiseuille flow theory predicts a nonlinear relationship between pressure and mass flow rate.

*Experimental Methods.* The apparatus used to study pressure-flow behavior in the IMO Prototype D device is illustrated in Figure 4.12. The apparatus consisted of a compressor to provide both a vacuum and positive pressure source, a mercury manometer for pressure measurement, and a mass flow meter (Top-Trak 821-1, Sierra Instruments, Inc., Monterey, CA). The Air Compressor had integral regulators to adjust the level of vacuum or positive pressure; the regulator on the helium tank enabled precise control of gas flow through the IMO (to be discussed later). Gas flow through the hollow fiber bundles was maintained in one direction for both positive and vacuum pressure experiments. A unidirectional flow path ensures that differences in the feed and exhaust manifolding of the hollow fiber bundles (to be discussed later) do

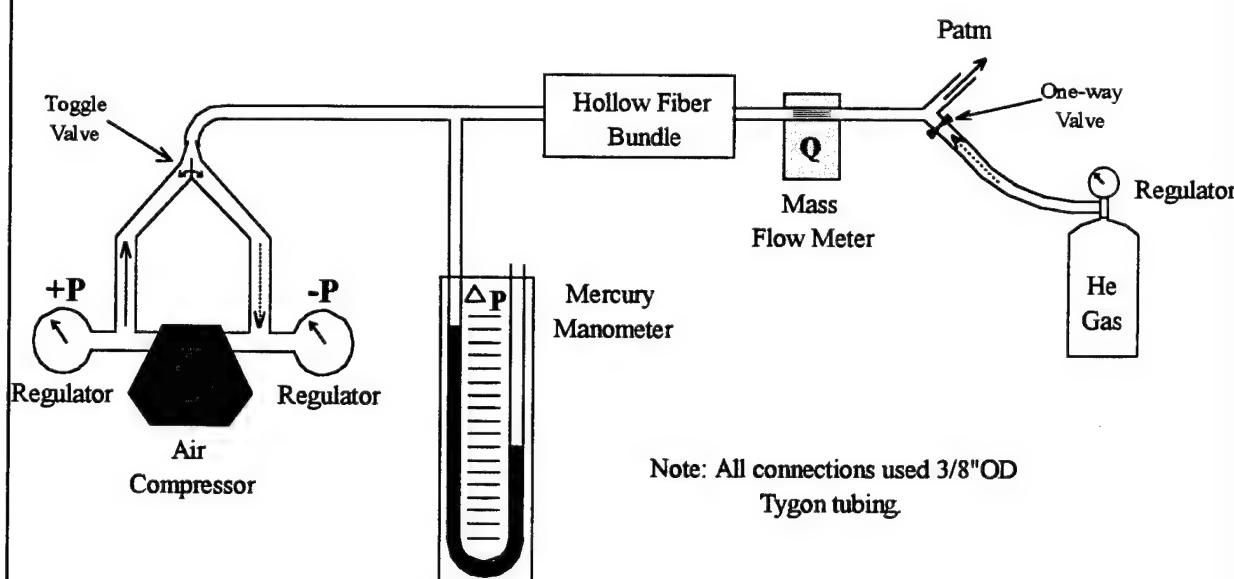


**Figure 4.12** Schematic of pressure-flow apparatus. The air compressor supplies both positive and negative pressure.

not translate into different flow patterns under vacuum and positive pressure.

The operation principle of the flow meter was such that it transduced mass flow rate and internally converted this reading to volume units ( $\text{lpm}^{\text{RTP}}$ ) at a reference temperature and pressure (RTP:  $T=25^\circ\text{C}$  and  $P=760\text{mmHg}$ ). The flow meter was placed at the atmospheric pressure end of the hollow fiber bundle for both vacuum and positive pressure experiments. Two resistance temperature detector coils around the flow probe chamber direct a constant amount of heat into the gas stream. The gas flow carries heat from the upstream coil to the downstream coil, and the resulting temperature difference (the output signal) is directly proportional to the gas *mass* flow rate. The flowmeter assumes  $\text{O}_2$  gas in determining mass flow rate so a calibration was done using a standardized rotameter (Model N092-04, Dakota Instruments, Monsey, NY) for room air and helium.

A typical pressure-flow experiment involved placement of the IMO device in the pressure-flow apparatus. The air compressor regulator was adjusted to provide a constant vacuum or positive pressure across the range of 0 to 400 mmHg. In helium vacuum experiments, a special procedure was followed to ensure that only helium entered the fiber bundles, and that the helium gas pressure at the entrance was near atmospheric pressure. As illustrated in Figure 4.12, a tee was placed distal to the helium supply tank. Vacuum pressure was then applied (using the air compressor) and the helium flow was increased until there was flow evident from the branch of the tee open to atmosphere.

**Pressure and Flow Results in the IMO** The principal evidence that compressibility can affect the gas flow dynamics within hollow fiber bundles is shown in Figure 4.13. The pressure drop versus mass flowrate relation was measured in the IMO device over the relevant range of gas flowrates (air flow). The measurements were done with flow driven both by vacuum and by positive pressure. Two principal features indicate departure from incompressible Poiseuille flow theory. First, the pressure drop - flowrate relation under both vacuum and positive pressure conditions show appreciable, consistent deviation from a linear relationship. (The curves represent second order regressions of the data) The second feature indicative of compressibility is that the pressure drop flowrate relationship differs between vacuum driven flow and positive pressure driven flow.

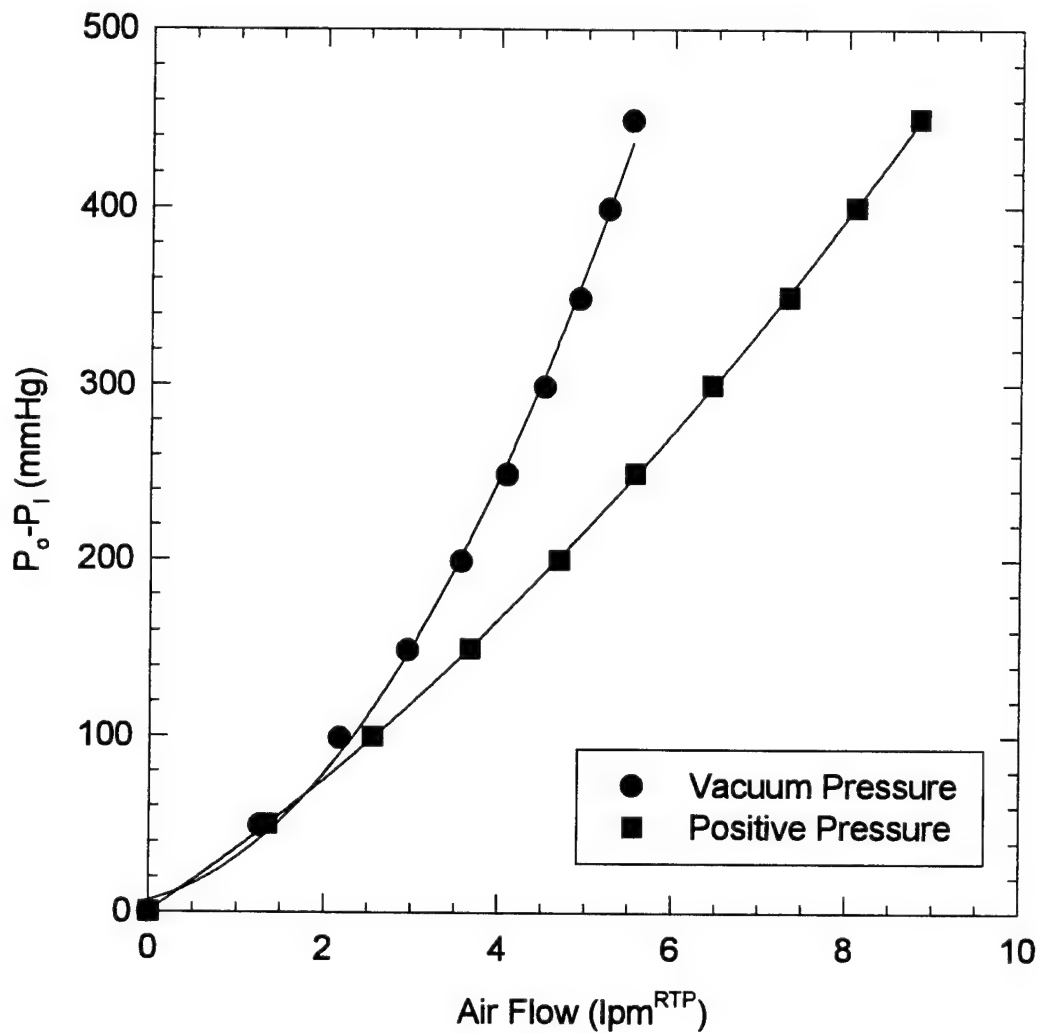


**Figure 4.13** The pressure drop versus flow measured in the IMO for air over a relevant range of flow rates. Measurements were done with flow driven by a vacuum and by positive pressure.

Application of compressible Poiseuille flow theory to the data is evaluated in Figure 4.14. Here, the pressure-flow relations shown in Figure 4.13 are recast according to pressure squared drop ( $P^2$ ) versus mass flowrate which, concordant with Eq. 4.5, should present a linear relationship, independent of pressure amplitude. In this "compressible Poiseuille" form, the pressure flow relations for vacuum driven and positive pressure driven flow do collapse more closely to a single relation, but systematic differences still exist. Furthermore, the relations show a clear departure from the linearity indicated theoretically. One immediate concern was that the flow resistance may not be constant, as assumed theoretically, but varies along the tube with pressure due to fiber compliance. We eliminated this concern, however, by repeating pressure-flow measurements under different ambient pressures imposed on the fiber bundle, and finding that the measured pressure-flow relations for the IMO device was independent of ambient pressure.

Inertial forces may also be contributing to deviations from compressible Poiseuille flow in the intravenous hollow fiber oxygenator; if so, the pressure-flow relations will depend on gas density. Accordingly, we repeated the vacuum pressure flow measurements for both air flow ( $\rho = 1.2 \text{ kg/m}^3$ ) and helium flow ( $\rho = 0.17 \text{ kg/m}^3$ ) through the hollow fiber ensembles. Pressure-flow results (Figures 4.15 and 4.16) are shown in incompressible and compressible Poiseuille flow form, respectively. Deviations between the pressure-flow relations for air and helium indicate that inertial forces are playing a role in the gas flow dynamics. Nevertheless, both the air and helium results follow the compressible flow theory (Figure 4.16) better than the incompressible flow theory (Figure 4.15). We can make relative comparisons by using the ratio of the second to first coefficients in the second order regressions imposed on the data. This ratio is 0.94 and 0.16 for air and helium, respectively, in the incompressible Poiseuille flow form and 0.13 and 0.032 for air and helium, respectively, in the compressible Poiseuille flow form. Thus, these results are consistent with the hypothesis that the pressure-flow behavior in our IMO device shows compressible Poiseuille flow behavior, but that inertial forces are playing a smaller but not negligible role.

The presence of inertial effects in the pressure flow relation for the IMO device may be problematical if these effects are associated with gas distribution at inlet and outlet manifolds.

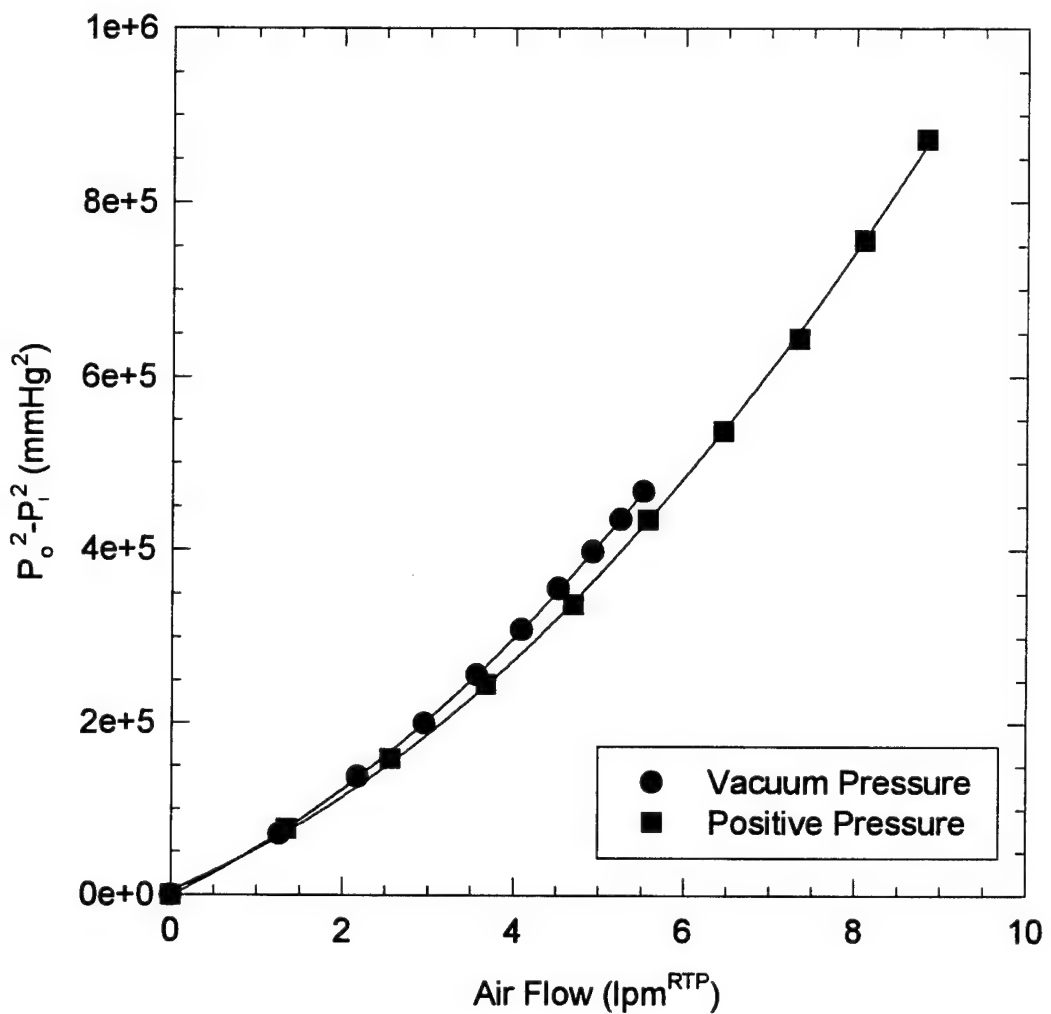


**Figure 4.14** Application of compressible Poiseuille flow theory to the pressure-flow data shown in Figure 4.13. In this "compressible" form, pressure drop expressed as pressure-squared drop.

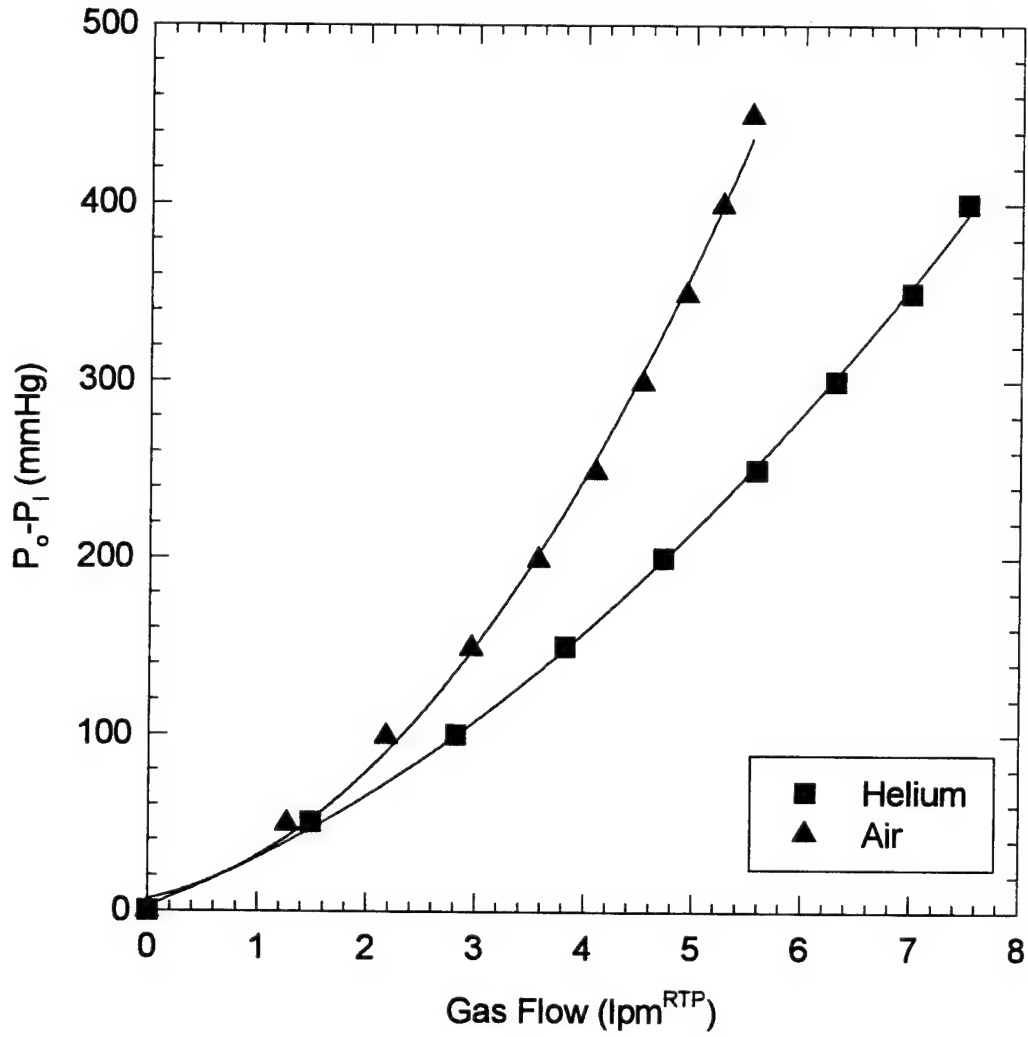


**Figure 4.15** The pressure drop versus flow rate relation measured in the IMO for air and helium flow driven by vacuum pressure. Results are expressed in the incompressible Poiseuille flow form.

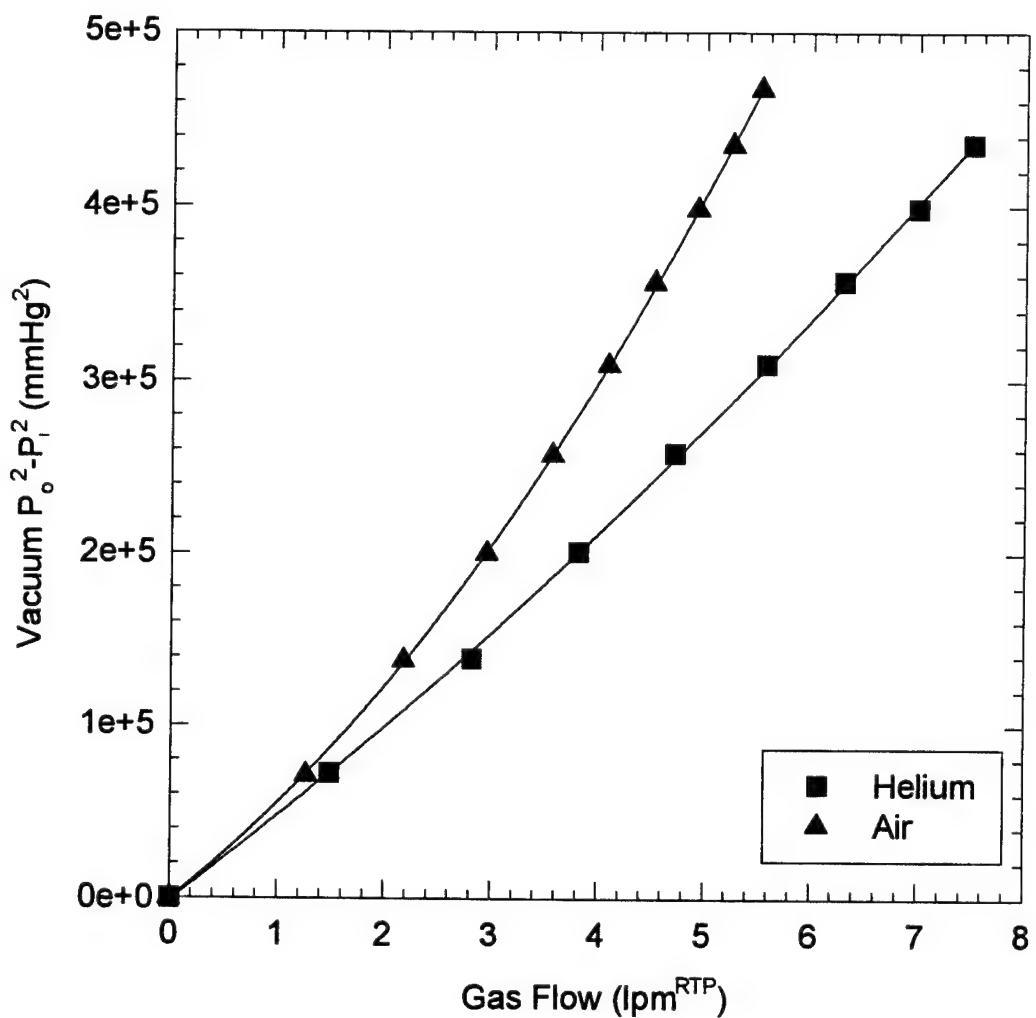


**Figure 4.16** The pressure drop versus flow rate relation measured in the IMO for air and helium flow driven by vacuum pressure. Results are expressed in the compressible Poiseuille flow form.

Assuming a volumetric flowrate of 10 l/min, the dynamic head associated with the fibers themselves is only 0.3 mmHg for air. Looking at the entire gas flow pathway within the IMO device, however, the largest dynamic head,  $\rho V^2$ , occurs in the feed tube ( $A = 0.016 \text{ cm}^2$ ) which supplies gas to the feed manifold leading to the individual fibers. For 10 L/min, the dynamic head associated with this tube is about 100 mmHg for air. Thus, inertial effects associated with flow out of this feed manifold may be responsible for the significant differences in the air and helium pressure-flow relations and the deviations from compressible Poiseuille flow theory (even the relatively small deviations for helium flow). We verified this by performing measurements on a test bank of the same hollow fibers as used in the IMO device, but with larger tubing leading to the distribution manifold to reduce the fluid dynamic head. These measurements exhibited negligible density dependence, and conformed well to compressible Poiseuille flow theory.

An appreciable dynamic head of gas entering a distribution manifold presents problems for uniform gas distribution to the individual fibers. This is so because as the fluid leaves the feed tube and enters the manifold the dynamic head is converted to static pressure. If the dynamic head is not a small fraction of the pressure drop across the fibers, then the potential exists, depending on the manifold geometry, for an appreciable nonuniform pressure distribution within the manifold and an uneven gas flow distribution through the fibers<sup>3</sup>. The potential problem for the IMO device is that fibers with low flow may not be effective gas exchangers, especially for CO<sub>2</sub> elimination. Thus, based on these pressure flow measurements in the Prototype D IMO, we will be modifying the gas feed pathway to reduce the dynamic head of the fluid as it enters the feed manifold. These modifications will reduce any potential for uneven gas distribution within the fibers constituting the device.

#### 4.5 Future IMO Prototype Development

The immediate focus of IMO development work in the next year will be on optimizing the gas pathways within the device. Most importantly, the helium delivery pathway will undergo

---

<sup>3</sup> Gas piping networks typically use diffusers to gradually reduce the dynamic head of gas streams before entering distribution manifolds.

further design review and modification aimed at improving balloon pulsation (filling/emptying) characteristics over a broader range of pulsation rates. Strict optimization of the helium pathway is a critical prerequisite to overcoming previous limitations to balloon- induced augmentation of gas exchange. The test apparatus designed and built to quantify the frequency spectrum of balloon pulsation provides an important tool for gauging improvements to the helium pathway. In addition, design review will also be done on the oxygen (and carbon dioxide) pathway through the IMO device. Of particular interest will be improving the manifolding from the feed tube to the fibers to reduce the dynamic head (momentum) of the gas and the potential for nonuniform gas distribution to the individual fibers.

Further work will also be done on enhancing gas exchange by direct mechanical activation of fiber movement. Pilot studies in this regard were especially promising, and a mechanical drive system has been designed and is being built to induce fiber movement over a broader range of frequencies. If further work shows equal promise, direct mechanical activation of fiber movement will be pursued in parallel to active balloon pulsation as a means for enhancing gas exchange in IMO prototypes.

We expect that with the ongoing focused development work and the expedient, standardized characterization testing of prototypes, candidate IMO prototypes will emerge over the next several months with gas exchange performance approaching our design goal. These prototypes will undergo more extensive characterization testing in the next year, consisting of a) *in-vitro* testing with blood in the mock loop, b) testing in an *ex-vivo* shunt model, and c) *in-vivo* acute animal testing.

Work has also recently begun on high performance computing as a tool for optimized design of the IMO device. This work is being pursued in collaboration with Professor Cristina Amon at Carnegie Mellon University. This effort will develop models, numerical methods, algorithms, and software environments for simulation-based characterization of gas exchange in the IMO device. Most importantly, these tools will become part of an optimized design procedure involving parallel computation and true gradient-based mathematical optimization, not trial and error repeated simulation. This will allow optimization of balloon and fiber design parameters (numbers of fibers, length of fibers, size of balloon, etc.), as well as operational parameters

(balloon pulsation amplitude and frequency, gas flowrate, etc.). The computer-based optimized design of an IMO will be a potentially invaluable conjunctive to the experimental development work. The effort is part of a multidisciplinary proposal on "High Performance Computing for Simulation-Based Artificial Organ Design" submitted recently to the National Science Foundation Grand Challenge program.

## 5. CONCLUSIONS

Further development of the University of Pittsburgh Intravenous Oxygenator (IMO) will focus on the Prototype D series device. The Prototype D series consists of a bundle of hollow fiber membranes manifolded to gas inlet and outlet lines, and a centrally located, helium activated balloon for augmenting liquid (blood) side mixing and gas exchange. Compared to other earlier IMO prototypes, the D series has a preferably smaller resistance to flow past it, and a configuration and size which is more compatible with peripheral venous insertion. Successful development of a Prototype D IMO requires strict optimization of balloon induced gas exchange augmentation.

Previous limitations to gas exchange enhancement with balloon pulsations (filling and emptying) have been traced to a pneumatically inefficient pathway for helium delivery. Theoretical and experimental analyses demonstrated that the pressure drop required for balloon activation exceeds that obtainable from the helium drive system (Datascope Intra-Aortic Balloon Console) even at moderate pulsation rates (80 bpm or less). Design review and modification of the helium pathway is ongoing. A special test and analysis was developed for quantifying balloon inflation/deflation over a broad range of frequencies. A prototype with a partially modified helium pathway has already been built and has shown effective pulsation at frequencies twice that of the unmodified prototype.

Direct mechanical activation of fiber motion has shown significant promise in a pilot study for enhancing gas exchange in IMO Prototype D devices. The level of gas exchange enhancement was greater than that with balloon pulsation (with the earlier, unmodified helium pathway) at the same rate of activation. A mechanical drive system is being developed to appropriately activate fiber motion over a broader range of frequencies. If further studies show promise, mechanical activation of fiber motion will be investigated as a parallel alternative to balloon activation for enhancing mixing and gas exchange in IMO devices.

The gas flow dynamics within the oxygen (and carbon dioxide) pathway have been analyzed theoretically and experimentally. The pressure flow behavior in this pathway shows an appreciable density dependence, which has been ascribed to the manifolding from the gas delivery tube to the hollow fiber inlets. The significant dynamic head of the gas entering this manifold may

engender nonuniform flow distribution through the fibers, which could reduce gas exchange. Accordingly, the potential for any such reduction will be eliminated by modification to the feed manifold.

The permeability of candidate hollow fiber membranes (HFM<sub>s</sub>) is being analyzed independent of IMO prototype studies. The apparatus, procedure, and data analysis have been developed to account for the contaminating influence of diffusion boundary layers on the fiber permeability measurement. Preliminary studies suggest that the commercially available MHF 200L (Mitsubishi Rayon) composite fiber may ultimately be unsuitable for IMO application because of a diminished permeability compared to totally porous HFM<sub>s</sub>. Other composite HFM<sub>s</sub>, however, are available that may be more suitable candidates, as may be custom coated fibers. These and other HFM<sub>s</sub> can be readily tested and evaluated with the fiber permeability apparatus.

## 6. REFERENCES

Brodkey, R. S. and H. C. Hershey, *Transport Phenomena, A Unified Approach.* New York: McGraw-Hill Book Co., 1988 (p. 383).

Conrad, S.A. et al. Major findings from the clinical trials of the intravascular oxygenator. *Artif. Org.* 18(11): 846-863, 1994.

Fazzalari, F.L., Bartlett, R.H., Bonnell, M.R., and Montoya, J.P. An intrapleural lung prosthesis: rationale, design, and testing. *Artif. Org.* 18(11): 801-805, 1994.

Grodins, F.S. and Yamashiro, S.M. *Respiratory Function of the Lung.* New York: Macmillan Publishing Company, 1978.

Hattler, B.G. et al. Respiratory dialysis: a new concept in pulmonary support. *ASAIO J.* 38:M322-M325, 1992.

Hines, A.L. and Maddox, R.N. *Mass Transfer. Fundamentals and Applications.* Englewood Cliffs, New Jersey: Prentice Hall, 1985.

Kamo, J. et al. A new multilayered composite hollow fiber membrane for artificial lung. *Artif. Org.* 14(5): 369-372, 1990.

Qi, Z. and Cussler, E.L. Microporous hollow fibers for gas absorption. II. Mass transfer across the membrane. *J. Membrane Sci.* 23:333-345, 1985.

Reeder, G.D. *The Biochemistry and Physiology of Hemoglobin.* Reston, Virginia: American Society of Extra-Corporeal Technology, 1986.

Vaslef, S.N., Mockros, L.F., Anderson, R.W., and Leonard, R.J. Use of a mathematical model to predict oxygen transfer rates in hollow fiber membrane oxygenators. *ASAIO J.* 40: 990-996, 1994.

Vaslef, S.N. et al. Computer-assisted design of an implantable, intrathoracic artificial lung. *Artif. Org.* 18(11): 813-817, 1994.

Weinberger, S.E. *Principles of Pulmonary Medicine.* Philadelphia: W.B. Saunders Company, 1992.

Williams, J.L., Federspiel, W.J. and Hattler, B.G. Gas flow dynamics in hollow fiber membranes. In preparation for *AIChE J.*, 1995.